Carbon/Graphene based interfaces and substrates for biocompatible photonic devices for living cells functional state monitoring

Hamza Rehman

Master Thesis

March 2020

Department of Physics and Mathematics
University of Eastern Finland

Hamza Rehman *Carbon/Graphene based interfaces and substrates for biocompatible photonic devices for living cells functional state monitoring*,
63 pages
University of Eastern Finland
Master's Degree Programme in Photonics

Supervisors Dr. Polina Kuzhir
MSc. Marian Baah

Abstract

Integration of mesenchymal stem cells, neurons or neuron tissue with non-biological sensor substrates makes great demands on the quality, physical and chemical properties of the materials used for the "neural interface", which broadly cover all elements of the interaction between the neural and artificial systems. Materials used for biophotonics sensing must provide cellular viability and stable functional state, preserve sterility and at the same time allow real-time analysis and control of environmental conditions and cellular activity. For the successful implementation of distributed sensor networks for living cells functional state monitoring first of all stable neuron–substrate interface should be developed. We concentrate on creation of biocompatible surfaces with a controlled roughness (for directed cell growth, creation of neural networks, etc), conductivity/insulating properties, photo-sensitivity made of graphene multilayers, pyrolytic carbon and graphitic films. One of the most interesting material for that purpose is graphene multilayers [1] and its more disordered counterpart, called pyrolytic carbon [2]. We study the influence of the synthesis conditions on the graphene/pyrolytic/graphitic films [3]. For the characterization, different spectroscopy tools like Raman, SEM and AFM tools were adopted. The effect of these films on the properties of the resultant bio-scaffold and finally the cell growth behavior on each of these bio-substrates were investigated.

Keywords: graphene; pyrolytic carbon; black silicon; CVD; evaporation; Copper; Raman; AFM; SEM; Bio-compatibility; glioma cells; roughness; hydrophobic; cell process

Preface

The research work performed in this thesis was carried out in the Institute of Photonics at University of Eastern Finland and the biological experiments part was done during my stay at Center for Physical Sciences And Technology (FTMC) Vilnius, Lithuania.

I would like to begin by expressing my utmost gratitude to my supervisor Dr. Polina Kuzhir for providing me with the opportunity to work on this research project. The support you provided and the resources you made available to my research work has been extraordinary. The guidance that you provided and the freedom of independently leading the research work has benefited me greatly and has developed in me the required skills and confidence to pursue professional research work confidently in the future.

Also, I would like to thank my co-supervisor Project Researcher Marian Baah for her untiring efforts throughout the duration of the thesis. With the practical hands on experience and knowledge that she possesses, she acquainted me with the techniques of nanofabrication. I would like to acknowledge the contribution of Professor Yuri Svirko who has been giving his invaluable insights into the research work and had always been very supportive from the very beginning. My special appreciation goes to the FTMC team especially Dr. Renata Karpicz and PhD researcher Elena Golubeva for an effective and friendly collaboration. Without their efforts, the successful implementation of this research would not have been possible. It was due to their guidance, planning and support that had made it possible for me to carry out the experiments within a timely manner. The abundant knowledge and research skills that Miss Elena Golubeva possess has really contributed to my research potential. I enjoyed the discussions that we had and it helped me to learn alot. Furthermore, i thank Dr. Seregey Malykhin for providing the graphene walls samples, Dr. Petri karvinen and PhD student Marina Fetisova for providing the bSi(UEF) samples and Dr. Ali Shah for providing the bSi(Aalto) samples. I am grateful to you all for providing me with a chance to be a part of this unique scientific work and i wish all of you success in future.

In the end, i thank my family and friends who have been always there to support me and motivating me from the very start. Last but not the least i thank my wife Dr. Ramsha who has always been there and stood steadfast by my side during the

thick and thin times. You have always been able to bring positive vibes in my life and have been pushing me to always give my best.

Contents

1 Introduction **1**

1.1 Modern applications of graphene and pyrolytic carbon in biosensing . 2

1.2 Overview 4

1.2.1 Graphene and Pyrolytic Carbon (PyC) 5

1.2.2 Electronic properties 5

1.2.3 Optical properties 7

2 Synthesis of Graphene, PyC **9**

2.1 Substrate preparation for the CVD synthesis 9

2.2 Chemical Vapour deposition 10

2.2.1 Graphene CVD mechanism 11

2.2.2 Types of CVD synthesis mechanism 12

2.2.3 CVD synthesis procedure 13

2.2.4 Role of Hydrogen in CVD process 16

2.2.5 Substrate effects on CVD process parameters 16

2.3 Graphene transfer process 18

3 Characterization of PyC/graphene coated substrates **21**

3.1 Raman Spectroscopy 21

3.1.1 Theory and working principle of Raman Spectroscopy 21

3.1.2 Raman spectroscopy measurements of PyC and graphene . . . 23

3.2 Scanning Electron microscopy (SEM) 24

3.2.1 Working principle of SEM imaging 25
3.2.2 Experimental details 27
3.3 Atomic force microscopy (AFM) 27
3.3.1 Working principle of AFM 27
3.3.2 Experimental details 28

4 Results and discussions **31**
4.1 Raman measurement 31
4.2 SEM image Analysis 37
4.3 AFM surface roughness study 39

5 Bio-compatibility test **49**
5.1 Cell culture 49
5.2 Fluorescent microscopy 50
5.3 Cells interaction with bio-substrate 50

6 Conclusions **55**

References **58**

Chapter I

Introduction

A biosensor monitors the degree of biological activity in terms of an electrical response [4]. In the field of medical science, the applications of biosensors are growing rapidly. Within a biosensor a transducer system can be either electrochemical, optical, acoustic, thermoelectric or ionic. However, the performance of a biosensor is largely based on the immobilization of the bio-component (cells). Furthermore, the efficiency of a biosensor depends on its chemical and physical properties such as impurities, thickness, temperature, stability of the materials, and most importantly its bio-compatibility [5]. Recently, in the field of biosensing alot of interest is put into the study of material interfaces with living cells. One of the main topics nowadays is the study of in-vitro cell culture on different substrates. Various materials are currently being studied in order to stimulate and detect signals from electrogenic cells like neurons [6]. Silicon was widely used in the implants for the monitoring and regeneration of neurons. Unfortunately, due to its non-biodegradable nature, silicon induced unfavorable reactions due to tissue scar [7] and the unstable mechanical and electrical results of the silicon implants led to research into other alternatives in order to overcome these limitations. A new generation of biosensors based on nanomaterials is currently being investigated. Such materials have interesting electrical and physical properties e.g high electrical mobilities, two-dimensional surfaces, 3D structures, porosity, bio-compatibility and biodegradability. Furthermore, in 1993 it was proposed to combine stem cells on nanomaterial based scaffolds due to these properties. Currently several natural and synthetic nanomaterials are being implemented for transplantation of stem cells (SC). For these SCs a scaffold is required to provide cell growth microenvironments. Moreover, it is the physi-

cal properties (impurities, surface roughness) and the chemical properties (surface charge, hydrophibicity/hydrophilicity) of these bio-platforms that controls the cell interaction. Other than that, the macroscopic, microscopic and submicroscopic variations in the topography of the substrate plays a vital role in the directional growth of the cells and their physical confinement [8].

Carbon-based nanomaterials are being considered as an ideal candidate in tissue engineering. The certain qualities of carbon nanomaterials which encourage its usage in the field of bio-engineering is due to the fact, that when injected into body, they do not trigger unwanted reactions, does not allow for blood clotting and exhibits good durability, strength and wear resistance [9]. Moreover, the biological molecules have special structures and with the help of these nanomaterials suitable platforms for purpose of neural tissue engineering can be created. Some of the carbon nanomaterials for this purpose includes carbon nanotubes (CNTs), carbon nanofibers (CNFs), glassy/pyrolytic carbon, single and/or multilayer graphene which may be in the form of 2D graphene sheet or a 3D foam structure. The interfacing of CNTs with biological molecules like DNA have been studied in [10], where the carbon nanotubes were chemically modified resulting in improved neuronal affinity and thus, enhanced neuronal cell growth.

1.1 Modern applications of graphene and pyrolytic carbon in biosensing

It is reported that Graphene related materials (GRM) promote the growth of stem cells into neurons which is a very attractive strategy for the treatment of neuronal injuries [11]. A number of studies have demonstrated GNs as bio-compatible substrates for growth and detection of different cells. It is noted that the electrical properties of single layer graphene (SLG) are sensitive to surface charge density, thus making it an active material for sensing applications. For the neural interfacing graphene is one of the most promising candidate. Due to its chemical inertness and extraordinary electrical properties, graphene have made possible detection of potential of electrogenic cells [6]. Recent studies have shown that graphene sheets can potentially act as bio-compatible, transferable, and implantable platform for SC culture. Moreover, it has also been found that as compared to uncoated surfaces, the graphene coated surfaces results in accelerated stem cell growth [12]. Comparison has been made

regarding the influence of graphene on stem cell growth by considering four different substrates with varying stiffness and surface roughness; Polyethylene terephthalate (PET), polydimethylsiloxane (PDMS), glass slide and SiO_2/Si substrate. The results unveiled that irrespective of the substrate, the main dependence of the stem cell growth is based on graphene [13]. Thus, suggesting that graphene can accelerate differentiation of human mesenchymal stem cells (hMSC). Reduced graphene oxide (rGO) is an option which has lower oxygen content than GO and has the advantage of lower cost of fabrication enhanced availability and better electrical conductivity. However, the defect density caused by functional groups in graphene-oxide (GO) affect its electrical conductivity and mechanical strength [11]. Compared to these graphene derivatives, pristine graphene offers better electrical conductivity and further enhances the electric field of the cell therefore, it has prospects of being used in cell culture and regeneration applications [14]. The neural stem cells are anchorage-dependent cells and requires good adhesion to the surface of the substrate. In [15] 3D graphene foam (GF) synthesized by chemical vapor deposition (CVD) is being considered. It is emphasized that the ripples and wrinkles that has resulted on the surface of 3D GFs allows for better interlocking of the cell with substrate and thus is able to proliferate and assist in the neural cell differentiation while at the same time being bio-compatible and showing no toxicity whatsoever. MSCs cultivated on graphene substrates maintain their morphology. Other than that, the high conductivity along with good bio-compatibility and long lasting chemical stability establish graphene and its other derivatives as the most favorable platforms for biosensors for in-vito environment [16].

Among other carbonaceous materials, Pyrolytic carbon (PyC) films have also gained alot of interest lately. These nanometer thick material consists of disordered graphene flakes. The bio-compatibility, robustness and durability has led to its applications in the biomedical field. Pyrolytic carbon implants have been already used in human bodies suffering from arthritis and no such side effects have been experienced by the trial subjects [17]. Furthermore, we will consider the two main carbon nanomaterials: Graphene and pyrolytic carbon (PyC) thin films.

1.2 Overview

In order to obtain an efficient biosensor a suitable material interface is required that encourages the adhesion and growth of the bio-component (cell). For this reason the main focus of this thesis is to develop different substrates and study their in-vitro bio-compatibilty. The structural variablity of the substrates plays a vital role in tuning of its bio-compatibility. Therefore, the effect of micro and nano topographical variations on cell growth and adhesion is studied in detail. In this work we will focus on understanding of carbon nanomaterials based bio-substrates for cell growth in order to achieve functional state monitoring of living cells. Focus will be on two carbon allotropes which are graphene and PyC. The presence of graphene and its disordered counterpart PyC on bio-substrate will be considered in order to direct the cell growth and adhesion. For this purpose we will be implementing different configurations of these carbon based interfaces including graphene on SiO_2(through Cu/Ni), perpendicularly oriented graphene walls on Si wafer, PyC on SiO_2 and PyC coated black silicon (bSi). The idea behind using bSi is that they have exceptional optical and electrical properties. The sample itself is sufficient to be used for Surface enhanced Raman scattering (SERS) analysis thus, providing the possibility of detecting very low number of molecules. The bSi provides the potential to develop base/sensor substrate itself. Moreover, compared to plain Si substrate, the bSi provides us with tunability of the the interaction of liquids with its surface which in turn can result in the achieving hydrophobic/hydrophilic nature of the bio-substrate [18]. The two differently manufactured bSi samples we will be considering are: bSi(Aalto) and bSi(UEF).

We will start by understanding the electronic and optical properties of graphene and PyC as a material itself. The topographical differences between graphene and PyC thin films will be under study. Chapter 2 focuses on the synthesis methods of graphitic carbon on different substrates, including Cu/Ni coated dielectric, bSi and direct deposition on quartz. The pre and post fabrication protocols and the effect of substrate on the synthesis conditions will also be discussed. Chapter 3 discusses the tools used in order to perform the structural characterization of the carbon based substrates after the synthesis has been done. In Chapter 4 results are presented from the different characterization tools like scanning electron microscopy (SEM), Raman, atomic force microscopy (AFM) in order to discuss the nanoscopic,

microscopic and macroscopic surface features along with the details regarding surface charge distribution. In chapter 5 the preparation of the bio-substrates as well as the cell growth and interaction behavior are studied. The comparison among all the fabricated prototypes will be made based on their surface morphology (including macro, micro, nano scale surface roughness) the thickness of the carbon material and the orientation effects on the biocompatibility of the substrate.

1.2.1 Graphene and Pyrolytic Carbon (PyC)

Graphene is a purely 2D structure consisting of sp2 hybridized carbon atoms arranged in a regular hexagonal order as shown in Fig. 1.1(a). A single graphene sheet has each carbon atom covalently bonded to 3 other carbon atoms. A bi-layer graphene consists of two sheets of graphene whereas a few layer graphene (FLG) can have upto 10 layers. The pyrolytic carbon (PyC) films consists of nanometer-sized randomly oriented graphene flakes of the linear size of a few nanometers [19]. Just like graphene this form of graphite also consists of sp2 hybridized carbon configuration.

1.2.2 Electronic properties

Graphene has relatively unconventional electronic properties which are determined by the carrier mobility $\mu = v/E$ where v is the Drude carrier Drift velocity and E is the applied electric field. It is reported that suspended graphene has a very high electron mobility of around 100,000 cm^2/Vs at room temperature being much larger than that of Silicon [21]. Mobilities of exfoliated graphene on SiO2-covered silicon wafer between 40,000 to 70,000 cm^2/Vs have also been recorded in [22]. Such high mobilities are accounted due to the fact that the electrons in graphene atoms are considered massless. Furthermore, the conductivity in graphene is directly proportional to the carrier density n which in turn controls the mobility, therefore, the mobility is limited by the scattering mechanism at different carrier density. The intrinsic mobility of graphene at room temperature is further affected by the scattering of the charge carriers with the phonons. However, the dominant phonon-induced scattering is due to the weak longitudinal acoustic (LA) phonons and even if these scatterings are available, the maximum achievable mobility of graphene at room temperature can still be around 200,000 cm2/Vs, accounting for far better mobilities reported by semiconductors [23].

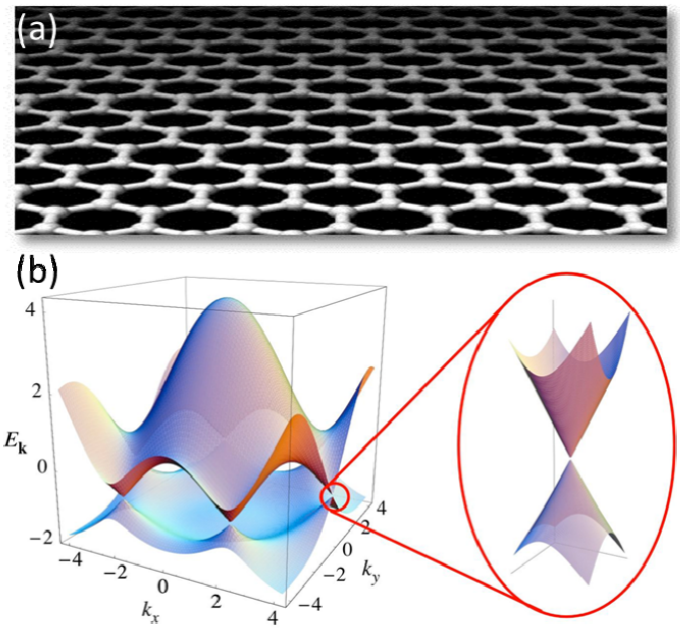

Figure 1.1: (a) 2D structure of graphene hexagonal lattice made of carbon rings connected by pi bonds (b) Dirac cone of graphene. The conduction band and valence band meet at the Dirac point. The dispersion relation is linear in the vicinity of this dirac point. [20]

The band structure of graphene is shown in Fig. 1.1(b), where the bandgap between conduction and valence band is infinitesimal. Moreover, both of these states are orthogonal and they touch at the Dirac point. For the electrical applications the band structure is approximated by two symmetric cones representing valence and conduction bands that are meeting at the Dirac points [24]. This representation is in contrary to other semiconductor materials where the energy dispersion relation follows a parabola. For graphene, the disperions relation in the vicinity of the Dirac point is considered to be linear. It is because of this linearity that graphene has much of its unusual electronic transport properties.

Evolution of electronic bands from zero band gap in case of pristine monolayer graphene to finite bandgap in case of multilayer graphene occurs. As a result, the electron mobility decreases as well as electrical conduction. Similar to semiconductors, graphene's electrical conductivity increases with the increase in temperature. Extremely high thermal conductivity of graphene has been recorded of approximately 3080-5150 W/mK. Moreover, the thermal stability and less thermal noise results in low Johnson noise, making graphene thermal management material in various electronic applications [25]. Furthermore, graphene has a constant bending stability. In [26] it is recorded that the 3D graphene foam made from a Ni nanowire foam maintains excellent electrical conductivity during 1000 cycles of folding process. Even though there is a 10 percent increase in resistance, the original resistance is recovered after release, thus, depicting excellent mechanical stability.

Properties of PyC mostly depends on its synthesis conditions [19]. From electronics point of view, PyC has interesting applications in microelectronics and can be used as a replacement to capacitors and cells for flash memory [27]. However, similar to graphene, PyC also shows good electrical and thermal conductivity in addition, it has a high chemical wear resistance and durability. These properties have led to the usage of PyC as a coating material [28].

1.2.3 Optical properties

Graphene in its pristine form is one-atom thick that results in strong absorption of $\pi\alpha = 2.3$ percent (where $\alpha = e^2/hc$ is the fine-structure constant) across the entire infrared and visible spectrum [29]. The broad optical absorption can be controlled by tuning the electronic Fermi level E_F. The transitions with energy below $2E_F$ are forbidden due to Pauli blocking whereas for energies greater than

$2E_F$, graphene is almost transparent. This strong electo-absorption effect is due to the graphene's unique electronic structure and its two-dimensionality [30]. Thus, allowing for graphene to be used as an active medium in electro-optical modulators. The photocarrier generation and relaxation processes in graphene are on a timescale of picoseconds which means graphene-based devices possessing operating speeds of 500 GHz and onwards [30].

The optical properties of the thin films are governed by the optical conductivity $\sigma_{OP} \approx 2\alpha/Z_o$ where α is the Beer-Lambert absorption coefficient [31]. Moreover, in case of graphene, the optical conductivity is independent of wavelength. PyC similar to its other allotropes like graphene and carbon nanotube (CNT) has a very strong absorption in the UV-IR region. This is mainly attributed to the dominating sp2 hybridization of carbon atoms and the π electrons [32]. In [18] the idea of coating of PyC on black silicon has been proposed in order to enhance the optical absorption of black silicon and suppress its reflectance in the IR range. Another interesting feature of PyC films is that its absorptivity and transmittivity is a function of film thickness. In [2] its demonstrated that PyC films as low as 75 nm are found to be capable of absorbing 50 % of incident microwave radiations. Therefore, PyC films find its applications in coatings on dielectric and metal substrates that can be used as optical enhancers, filters and shields.

Chapter II

Synthesis of Graphene, PyC

In this chapter we will be discussing in detail about the fabrication steps for the synthesis of single and multi-layered graphene on Cu/Ni foils and dielectric substrates. Also, the synthesis of pyroloytic carbon (PyC) on dielectric substrate and/or black silicon will be discussed. Furthermore, the steps involved in the pre and post synthesis process will be also highlighted.

2.1 Substrate preparation for the CVD synthesis

Graphene and PyC were synthesized on different substrates and the methods for the preparation of these substrates were different. Therefore it is imperative to understand the method of preparation of these underlying substrates. Below are the brief details of the methods by which these substrates were prepared.

Cu/Ni film on SiO_2 : Both Cu and Ni atoms were deposited by physical vapour deposition (PVD) technique. Two different approaches were employed namely sputtering and evaporation. For the sputtering of Cu/Ni atoms onto the SiO_2 substrate we used the magnetron sputter EMITECH (KM675-X). On the device, the parameters were set as follows: Material: Cu (density: 8.96 g/cm^3). A 400 nm thick layer of Cu was deposited whereas, 30 nm of Ni was deposited on quartz wafer of 0.5 mm thickness.

Also, via thermal evaporation method, Cu films were deposited using the the thermal evaporator UNIVEX 300. Tungsten elongated dimple boats were used. Within these boats, the metal pellets were placed of the same materials, respectively. The quartz wafers were placed inside the vacuum chamber. The current was supplied

to cause the melting of the metal pellets and being evaporated onto 0.5 mm thick quartz wafer. With this technique, Cu and Ni film thickness of 400 nm and 43 nm were deposited, respectively.

Cu/Ni foils: Commercially available copper foils with a thickness of few microns were used. Similarly, high quality Ni foils with thickness of 2.5 μm was used for the CVD synthesis of graphene.

Black Silicon (bSi): bSi subsrates were provided by Department of Micro and Nanosciences, Aalto University, Espoo, P.O. Box 13500, FI-00076, Finland [33]. The fabrication details of the bSi substrates can be found in the PhD thesis [34]. Firstly, plasma enhanced chemical vapour deposition (PECVD) was employed for the deposition of SiO_2 mask material for the later pattering of bSi. For this, Oxford instruments Plasmalab80Plus was used. As a precursor SiH_4 and N_2O were used for the SiO_2 deposition. This process was carried out on a 100 mm thick wafer at 300 °C and pressure of 100 mtorr.

The patterning of the oxidized Si wafer was done by spin coating photoresist AZ5214E at 4000 rpm for 1 minute. The photoresist-SiO_2 was pre-baked at 95.5 °C after which the coated wafer was patterned using UV exposure.

The patterned SiO_2 with the photoresist mask was dry etched. The etching was performed in Oxford Instruments Plasmalab80plus plate with water cooled graphite biased substrate. For this process CHF_3 and Ar were used at 25 sccm and 5 sccm, respectively and at a pressure of 30 mtorr. Finally the fabrication of bSi was carried out with Oxford Instruments Plasmalab system 100-ICP180 which has double plasma source that allows for independent control over density and directionality of ions. The plasma is created at a pressure of 100 mtorr within the temperature range -150 to 400 °C. Tall black Si pyramid like structures were obtained at pressure of 10 mTorr with SF_6 flow rate of 40 sccm, O_2 flow of 18 sccm at -110 °C for 7 mins, followed by 7 minutes of etching.

2.2 Chemical Vapour deposition

Chemical vapour deposition (CVD) is the process for the deposition of thin films of different materials. The general process flow of the CVD deposition is given in

Fig. 2.1. The substrate, which is usually a transition metal element, is brought into

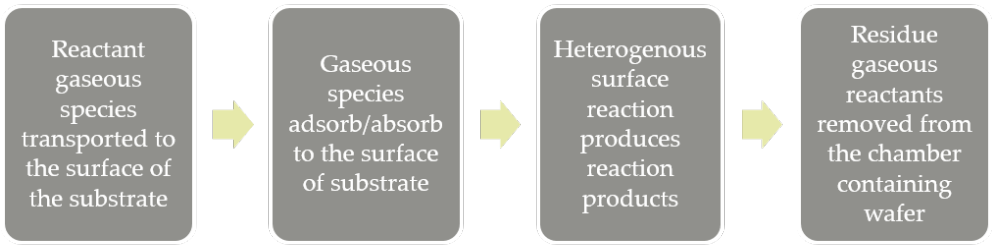

Figure 2.1: Process flow of CVD mechanism

contact with one or more precursors at a particular temperature and pressure. A catalytic reaction takes place where the precursor gas react and decompose onto the substrate surface and deposition of the required material is obtained.

For the wafer-scale graphene the catalytic chemical vapour deposition techniques is highly favorable. Moreover, there are other techniques to obtain graphene sheets such as mechanical exfoliation of graphite and the epitaxial growth from SiC. However, these techniques are not suitable for mass graphene fabrication and obtaining high quality graphene with atomically flat surfaces [35]. CVD on the other hand allows for easier, cost effective, scalable, mass production and transfer of the graphene onto the desired substrate. A significant advantage of this technique is that this process can be done on a large scale while maintaining the large-area homogeneity

2.2.1 Graphene CVD mechanism

The process involves the thermal decomposition of the carbon-based precursor such as methane given by the below equation:

$$CH_4(g) \longrightarrow 2H_2(g) + C(s) \tag{2.1}$$

There have been different reports regarding various transition metals being used as substrates for the growth of graphene including Cu, Ni, Co etc [35].

2.2.2 Types of CVD synthesis mechanism

In [36] two different mechanisms for the CVD synthesized has been proposed. As shown by Fig. 2.2 CVD processes are further classified into two mechanisms. Mech-

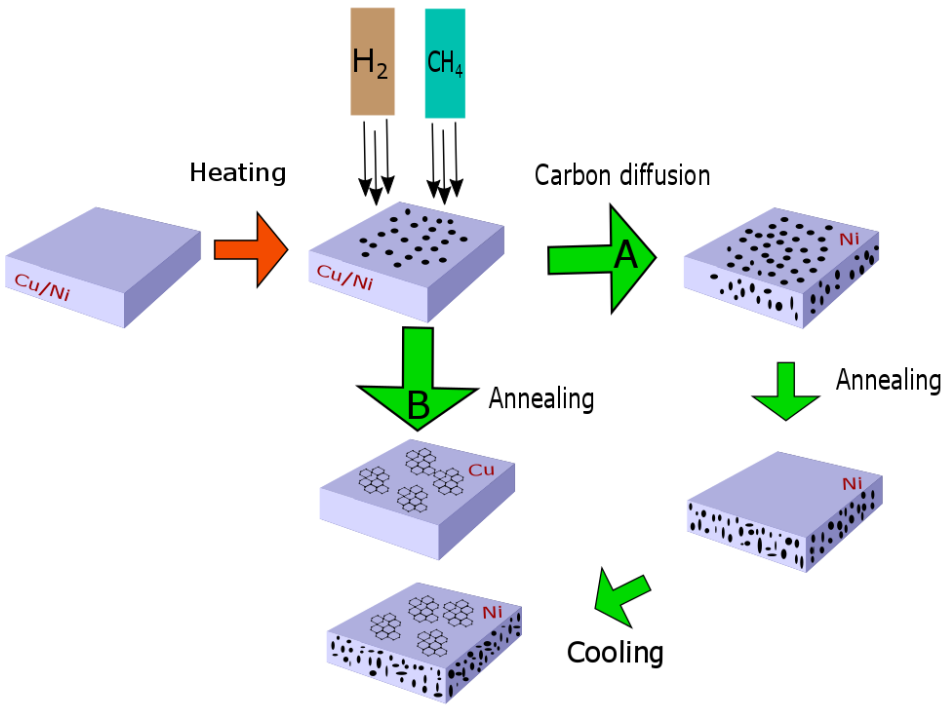

Figure 2.2: CVD Graphene growth mechanism on Ni and Cu substrates: (A) represents the dissolution of carbon atoms into the Ni bulk metal and then precipitation during the cooling stage, (B) represents the direct deposition of carbon atoms on surface of Cu.

anism (A) is Bulk mediated growth which consists of two steps i) dissolution of the carbon atoms into the bulk metal (e.g. Ni) at high temperature (800 °C-1000 °C)

and ii) carbon atoms precipitate/segregate onto the surface to form graphene. The step two may be simultaneously taking place during the annealing and the cooling stage of the CVD process. Whereas in the surfaced mediated growth mechanism represented by (B) shows that the carbon atoms are directly deposited on the surface of the catalyst (e.g. Cu) substrate and thus forming graphene layer without any precipitation step [35]. However, the precipitation/segregation is the dominant mechanism that is followed by most of the transition metals for the catalytic graphene growth. As the solubility of carbon is very low in Cu therefore, it facilitates the surface growth mechanism and leads to formation of single layer graphene [37].

2.2.3 CVD synthesis procedure

The CVD process was carried out using Carbolite thermal Low Pressure CVD (LPCVD) furnace as shown in Fig. 2.3. The substrate was placed onto the sample

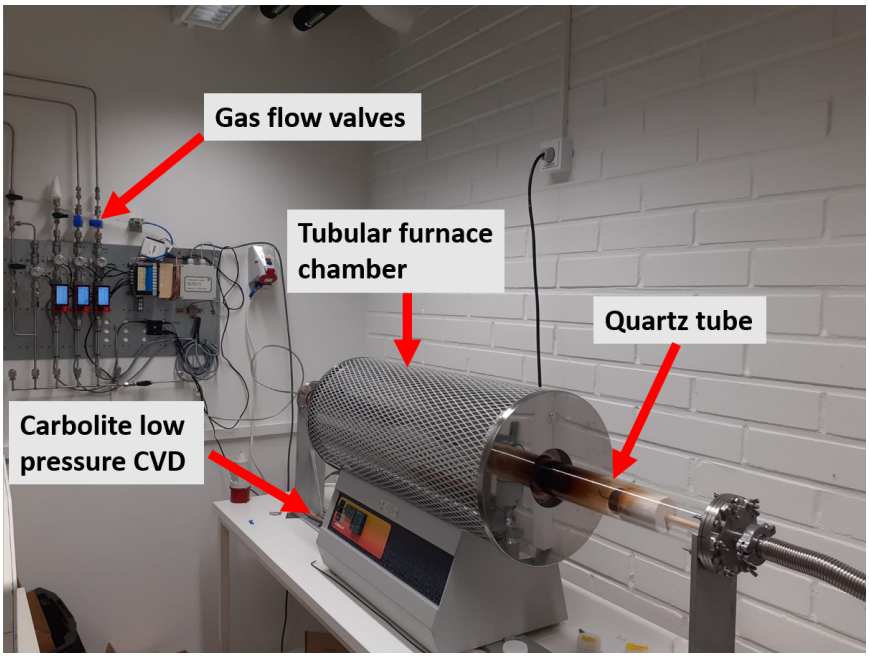

Figure 2.3: Carbolite low pressure CVD at University of Eastern Finland. This setup was used to synthesize the graphene and PyC on different substrates.

holder and inserted into a quartz tube. The setup schematic is represented by the

Fig. 2.4.

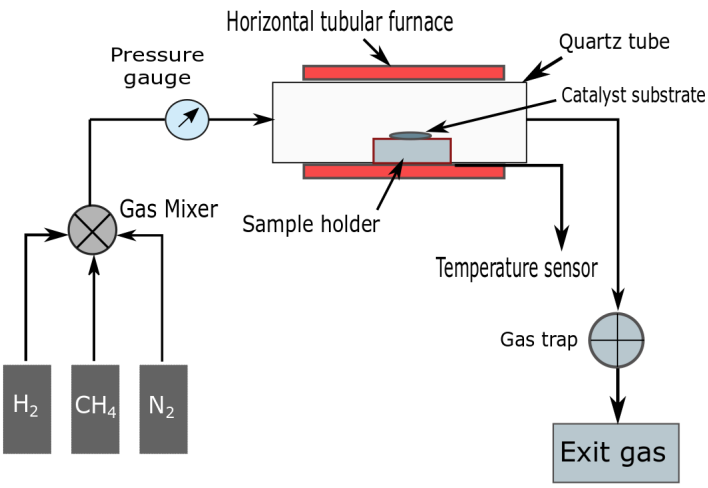

Figure 2.4: Set up schematic for CVD graphene synthesis.

Graphene on Cu/Ni SiO_2: The substrates with coated Cu/Ni films (2 x Cu: 400 nm, 1 x Ni: 43 nm, 1 x Ni: 30 nm thicknesses) prepared previously were used. The chamber was sealed with the vacuum pressure set to 0.8 mbar. At such low pressure the diffusion of the gas decreases and so the precursor gases approach the substrate more closely and the deposited films have better uniformity and homogeneity. Initially only the H_2 gas is allowed to flow within the chamber for up to 2 hours. Afterwards, the furnace was heated up at different heating rates. First the temperature is raised till 700 °C at ramp of 20 °C/min. From there onwards the step size was changed to 10 °C/min. Once the temperature reached 1000 °C (800 °C for Ni) the sample was annealed during dwelling stage for 1 hour. This temperature is selected so that it is well below the melting point of the catalyst substrates used and thus only causes the softening of the boundaries. For the first 30 minutes of this stage only H_2 was present and the last 30 mins CH_4 was also added into the chamber. This duration during the annealing stage ensures that the carbon atoms are uniformly distributed within the Ni film. The ratio of hydrogen to CH_4 was 1 to 2 (H_2: 10 sccm, CH_4: 20 sccm). After 1 hour the H_2 was left while the CH_4 flow was stopped. With a gap of 2 minutes the vacuum pumping was stopped and

the chamber was left with only static H_2 inside. During this step, H_2 carries away any excess carbon atoms out of the chamber. The chamber pressure was allowed to increase to 5 mbar after which H_2 flow was also stopped. The heating element was turned off and the temperature was reduced to 700 °C at a rate of 10 °C/min and the chamber was left to cool on its own overnight.

Graphene on Cu/Ni foils: The process performed for graphene CVD synthesis on Cu/Ni foils is much the same as for that for Cu/Ni on quartz. However, in the case of Ni higher temperatures are needed in order to obtain high quality graphene therefore the CVD was carried out at 1000 °C. This is because the process was initially carried out at 800°C but not so high-quality graphene could be obtained.

Graphene walls on Si (Gr-wall (285)): The graphene walls coated on Si substrate were provided by Dr. Sergei Malykhin from University of Eastern Finland. The samples were produced on silicon substrate by plasma-assisted CVD process. A mixture of CH_4-H_2 was used in the presence of d.c discharged activated plasma. The deposition process was carried within the temperature range 850 °C - 1100 °C with pressure range of 8.5-9 kPa and this process lasted for about 45 minutes [38]. These graphene walls are fabricated such that they are oriented perpendicular to the Si substrate.

PyC/SiO2 and PyC/bSi: The PyC films were deposited via CVD on the SiO_2 or bSi substrates that were prepared previously. Initially, the CVD chamber was sealed with the sample substrate inside and H_2 was pumped for 2 hours at flow rate of 20 sccm and 1 mbar pressure in order to clean the substrates. Next, the pumping was stopped and with the H_2 flow the chamber pressure was increased to approximately 10 mbar. From there onwards H_2 flow was stopped and the CVD chamber was heated till 700 °C in static H_2 environment. With H_2 already inside, CH_4 was injected into the chamber at 50 sccm, allowing the chamber pressure to reach approximately 24.4 mbar. The chamber was further heated till 1100 degrees Celsius at a rate of 10 °C/min. Throughout this process there was no active flow of gasses and the entire process was done in static conditions. Dwelling for 5 minutes was allowed and then cooled down to 700 °C at rate of 5 °C/min. Once 700 °C of

temperature was obtained, CH_4-H_2 mixture was pumped out and replaced with H_2 (20 sccm) at 10 mbar. Overnight cooling was allowed in these conditions.

2.2.4 Role of Hydrogen in CVD process

The role of H_2 is very crucial as it eliminates the impurities which may cause local variations of carbon solubility that may affect the local graphene thickness. H_2 also acts as an activator for the successive hydrogen abstraction of CH_4 by H atoms as shown by Eq. 2.1 and thus, leading to formation of methyl radicals CH_3 which adsorbs onto the surface of the catalyst. This surface bound carbon is necessary for the graphene growth. Furthermore, the hydrogen also plays an important role for the transition from sp^3 to sp^2 configuration [39]. Also, during the cooling stage it acts as an etching agent and removes any weaker carbon bonds which may result in defective graphene [35].

2.2.5 Substrate effects on CVD process parameters

Copper: the ways of optimization

Properties of the catalysts used for CVD has a major influence on the graphene growth. The decomposition of the carbon precursor is assisted by the catalysts with certain activation energy. This energy is provided in the form of temperature. Different transition metals have different activation energies and thus, this controls the operating temperature for the CVD process. Carbon solubility in these metals is temperature dependent. Cu has a very low carbon solubility of about 0.001 percent at 1000 °C The low solubility is due to the filled 3d orbital, resulting in lower tendency of the adsorption of carbon atoms on its surface. Therefore, a CVD process temperature of 1000 °C is preferred in order to support the formation of single layer graphene However, it is still possible to obtain low quality graphene at temperature of 800 °C [40]. In the case of Cu, the graphene growth is a self-limiting process which means that the growth process terminates once the surface of the metal substrate has been completely covered with a monolayer graphene, thus gradually the catalytic activity dies out [35]. This is possible only under very low-pressure CVD. Whereas, under ambient pressure non-uniform multilayer graphene is formed.

The CVD process for Cu/SiO_2 was repeated with different thicknesses of the

deposited Cu layer by both evaporation and sputtering techniques using the equipment UNIVEX-300 and EMITECH (KM675-X), respectively. The process has been already described in Chapter 2 where substrate preparation for the CVD synthesis has been discussed. Initially, 50 nm of film was deposited, and it was found that after the CVD process almost all the Cu layer has been sublimed and correspondingly no significant graphitic peaks were observed during Raman measurements. This fact is supported by [41] where it is mentioned that during the annealing stage there is loss in the copper surface by sublimation. The process was repeated with 200 nm and 400 nm thickness of Cu layer and it was observed that even with a thickness of 200 nm, only amorphous carbon was obtained. However, with 400 nm of Cu we were able to obtain a form of graphitic carbon with distinguishable D, G and 2D Raman peaks.

Nickel

Nickel has a comparatively higher carbon solubility (0.9 percent at 900°C). This is mainly because Ni has non-filled d orbitals that enhance its ability to adsorb the gaseous carbon precursor. The temperature dependent solubility (S) of the carbon atoms in Ni is governed by the following equation [42]:

$$S = S_0 \exp(H/kT), \tag{2.2}$$

where S_0 represents the entropic pre-factor and the value H = -0.42 eV is the heat of precipitation and k is the Boltzmann constant with value = 8.6173324 x 10^{-5} eV K^{-1}.

As previously mentioned, the main mechanism for graphene growth on Ni is via surface segregation method, where the carbon atoms diffuse into the Ni bulk during high temperatures and then precipitate/segregate out on the Ni surface during cooling period [36]. The diffusion coefficient (D) of carbon atoms in Ni is thus, represented as [42]:

$$D = D_0 \exp(-E_D/kT), \tag{2.3}$$

where D_0 = 2.48 $cm^2.s^{-1}$ is an entropy pre-factor and E_D=1.74 eV is diffusion activation energy.

Usually multilayered graphene is formed on Ni surface, however, monolayer graphene is also possible by varying the cooling rate. A higher cooling rate will

allow limited amount of carbon to diffuse out to the surface. Another way is to polish the surface of nickel with longer annealing time which will result in fewer grain boundaries and thus, limiting the nucleation of multilayer graphene [43]. Whenever the nucleation site is activated, carbon atoms in the surrounding grains are pumped out and thus, a diffusive flux of carbon atoms towards the nucleation site is established causing redistribution of carbon inside the Ni [42]. The as-grown graphene formed on Ni is in the form of small individual islands that are clearly distinct with different thicknesses [35]. This is mainly due to the presence of the grain boundaries (GB) with varying radius of curvatures. These grain boundaries act as "carbon drains " and are the preferential precipitation sites. At these locations the carbon accumulates to form few layer graphene (FLG) and as well as graphite [42].

2.3 Graphene transfer process

After the CVD process, the as-grown graphene on metal coated dielectric is separated from the underlying catalyst substrate and obtain the graphene on dielectric substrate. The detailed process flow is shown in the Figure 2.5.

Spin coating: In order to prevent the graphene from being dissolved away during the etching process, a thin layer of PMMA (ARP 642.09) was spin coated onto the as-grown graphene at 1500 rpm for 60 seconds. At this speed, we will get PMMA thickness of 0.3 um. The thickness of this layer must be such that it provides the mechanical strength to support the graphene structure.

Baking: The PMMA/graphene/catalyst-substrate was then baked at 150 degree Celsius for 5 minutes by placing it on the hot plate (ATV tech HR300) with the PMMA-Gr side on top. This process is useful for making sure that the PMMA and graphene is properly adhered to each other.

Wet etching: The PMMA-Graphene thin film was released from the catalyst substrate by placing in an etching solution. The etching solution used for Cu and Ni are FeCl3 and CuS04, respectively. In order to remove the Ni, the etching solution of 10 g CuSO4 : 50 ml HCl : 50 ml deionized water was used. The sample was left in this solution overnight. After removing them from the etching solution they were

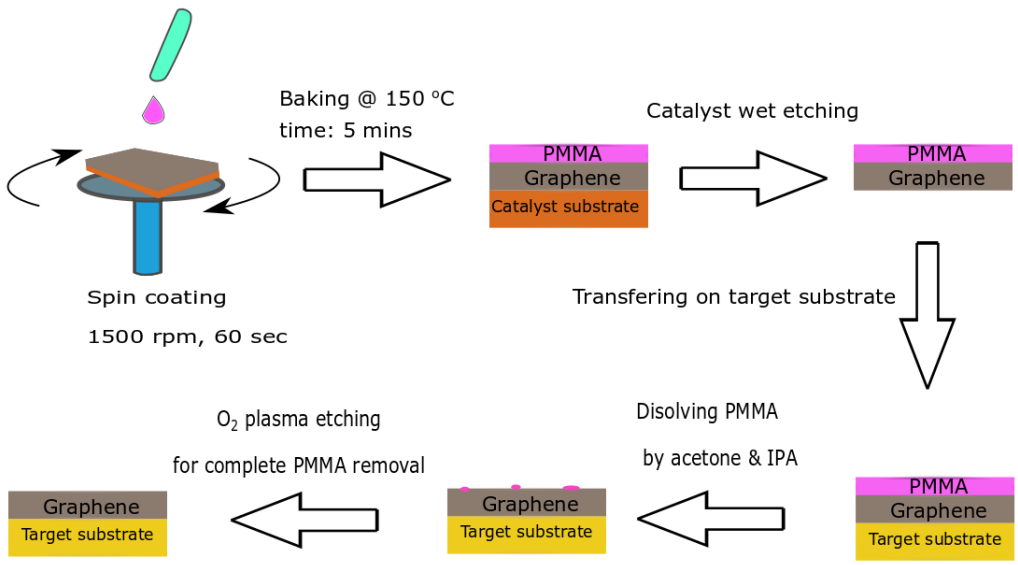

Figure 2.5: Sequences of as-grown graphene transfer by PMMA method and cleaning by plasma etching.

rinsed in deionized water and then dry with compressed nitrogen gas. For removing Cu from the PMMA/Gr/Cu/$Si0_2$, we first scratched a little surface on the sides in order to expose the Cu to the etching solution. Then the sample was placed in HCl and H_20_2 solution and left overnight. However, Cu was not removed completely contrary to Ni.

Dry etching: The PMMA-Gr-substrate proceeded for dry etching. The equipment used was oxygen plasma (MARCH CS1701) with RF source (ENI) as shown in Fig. 2.6. This step removes any unnecessary PMMA molecules that may have been left after dissolving in acetone and IPA solution.

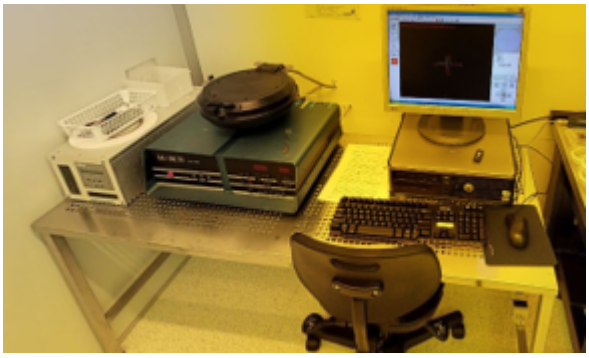

Figure 2.6: Oxygen Plasma (MARCH CS1701) with RF source used in dry etching in order to remove any leftover PMMA.

Chapter III

Characterization of PyC/graphene coated substrates

In this chapter, we will discuss thoroughly the tools that were used to characterize the synthesized carbon-based substrates. The underlying working principle of these tools and the parameter settings will also be mentioned.

3.1 Raman Spectroscopy

Raman spectroscopy is a tool that is used for the characterization of crystalline, nanocrystalline, and amorphous material [44]. This method provides the fingerprint of the molecular bonds and the crystalline structure through non-resonance excitation of vibrational modes within the molecule.

3.1.1 Theory and working principle of Raman Spectroscopy

The underlying phenomena that the Raman spectroscopy technique operates on is the Raman effect or Raman scattering. This phenomenon was discovered in 1921 by Chandrasekhara Venkata Raman (named after him). He observed that there is change in the scattered light with respect to the incident light in several organic molecules and was thus published in his work, *A New Type of Secondary Radiation*, in 1928. This effect is termed as the Raman effect of Raman scattering and the study and analysis of this effect is called Raman spectroscopy

The principle of the Raman effect involves the light-matter interaction where the incident light is inelastically scattered by irradiated matter [45]. Fig. 3.1 shows the three different types of scattering processes when light interacts with matter where $h\nu_0$ and Ω_s represent photon energy and the scattering frequency shift, respectively.

Figure 3.1(a) represents the Rayleigh scattering, which is an elastic collision and

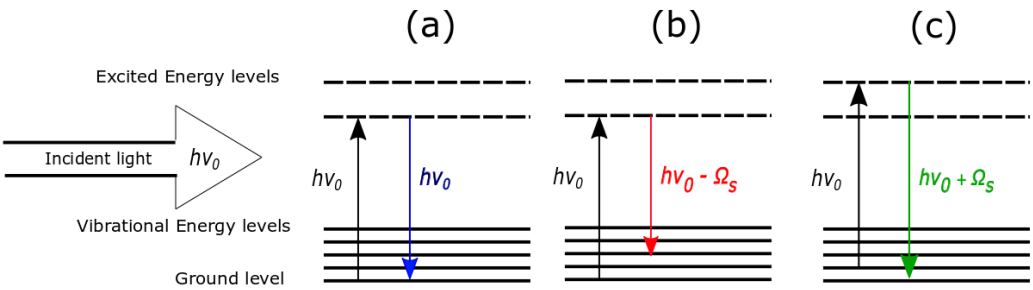

Figure 3.1: Illustration of Rayleigh and Raman scattering processes: (a) Rayleigh scattering (b) Stokes Raman scattering (c) Anti-Stokes Raman scattering. Here $h\nu_0$ is the energy of photon and Ω_s represents the scattering frequency shift.

where no change in frequency or wavelength of the photon and thus no energy transfer takes place. Figure 3.1(b,c) on the other hand represents the Raman scattering where there is change in photon energy level. In this process either photons absorb or emits energy. The energy of the photons from the laser are shifted up or down and this gives information regarding the vibration modes in the system. The phenomena for this process is termed as Raman scattering, which can be further classified into two types; Stokes and Anti-stokes scattering [46]. In Stokes scattering, as shown by Fig.3.1(b) the excited photon lands at a higher energy level than the initial energy level and the emerging scattered light has a lower frequency than incident light. Whereas, in the anti-Stokes Raman scattering, the excited photons land at a lower energy level than that of initial energy level. Thus, resulting in the scattered light having lower photon frequency than that of incident light, represented by Fig.3.1(c). The Raman spectra gives the relation between intensity of the scattered light and the wavenumber or also known as Raman shift (cm^{-1}) and is given by

$$\textbf{Raman shift} = (\frac{1}{\lambda_{incident}} - \frac{1}{\lambda_{scattered}})\mathbf{x}10^7, \tag{3.1}$$

where both λ are wavelengths with units nm.

3.1.2 Raman spectroscopy measurements of PyC and graphene

The Raman spectra of graphene and its disordered counterpart PyC all possess three distinct peaks namely the first order D (disorder) peak (1333 cm^{-1}), the G modes (1578 cm^{-1}) and the second order 2D mode (2682 cm^{-1}). The G mode, is due to the high frequency E_{2g} phonon mode which is Raman active and is caused by the in-plane vibration of carbon atoms as shown in Fig. 3.2 This mode is allowed for all sp2 hybridized carbon networks. The D mode can be described as an in-plane breathing vibration mode of the hexagonally arranged carbon rings, represented by Fig. 3.2, and this mode is activated by presence of defects [47]. The 2D mode, also known as G' band, on the other hand is always allowed and is the most intense feature for a single layer graphene. However, it should be noted that just like D band the 2D band is also excitation wavelength dependent and therefore it is important to know the excitation wavelength while carrying out the measurements. With the

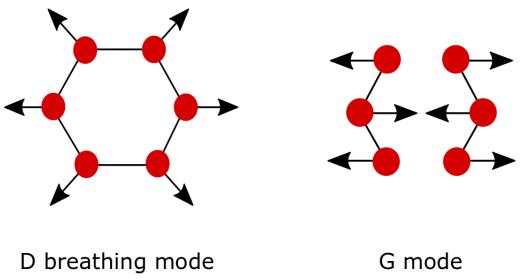

Figure 3.2: Motion of carbon atoms as a result of D and G vibrational modes.

help of certain Raman markers, extensive structural characterization of carbon based materials can be performed. For example, the intensity ratio I(D)/I(G), quantifies the defects in the carbon-based structure. Furthermore, the ratio I(2D)/I(G) along with the FWHM(2D) allows for the identification of number of graphene layers. However, during this calculation the nature and the surface charge density of the substrate should be considered. The shift in the G peak gives us information about stress/strain, deformation, pressure and temperature variations experienced by the structure. While, FWHM of the G peak gives a measure of the crystallinity, defects

and doping of the graphitic carbon [48]. Furthermore, the distance between defects L_D(nm) and the point defect density $n_{\mathbf{D}}$ (cm^{-2}) at any excitation wavelength can be found by the following equations [49]

$$L_D^2 = (1.8 \pm 0.5)\mathbf{x}10^{-9}\lambda_L^4(\frac{I(D)}{I(G)})^{-1}, \tag{3.2}$$

$$n_D = \frac{(1.8 \pm 0.5)\mathbf{x}10^{22}}{\lambda_L^4}\frac{I(D)}{I(G)}, \tag{3.3}$$

where λ_L is the excitation wavelength and I(D) and I(G) represents the relative intensities of the D and G peak, respectively.

Experimental setup

Raman measurements were performed at University of Eastern Finland, Finland and Center For Physical Sciences And Technology FTMC Vilnius, Lithuania using Raman spectrometer/microscope inVia (Renishaw, UK) as shown in Fig. 3.3 and comes with its custom PC software WIRE. Excitation wavelengths of 514 nm and 785 nm near infrared (NIR) laser source with initial power of 100 mW were used for all the samples. The grating used for 785 nm laser had 1200 line/mm. Using the WIRE software, the spectral acquisition parameters were set. Accumulation time and exposure time were each set to 10 seconds. Whereas, the laser power was set to 1 percent of the total incident laser power with a lens objective of x50 magnification

3.2 Scanning Electron microscopy (SEM)

The principle of electron microscopy (EM) is similar to that of an optical microscopy (OM) but instead of a visible light source, the EM uses a source of highly energetic electrons [50]. The main limitation of an optical microscope is the diffraction limit d = $\lambda/(2n \sin \Theta)$ in the visible wavelength range (λ = 200 nm to 750 nm). Whereas, with electron microscope higher resolutions are possible due to the very short wavelengths of the electron (0.37 to 8.59 nm) [51]. This allows for resolving of the atomic features down to micro and nanometer scales. Other than that EM has better depth of focus than OM and so more suitable for studying the surface roughness.

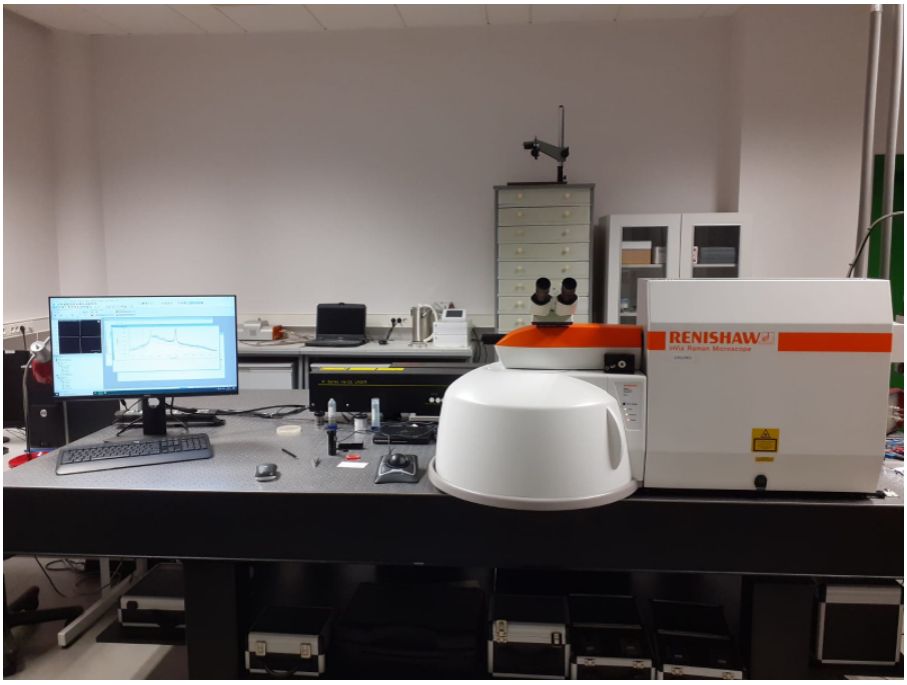

Figure 3.3: Raman spectrometer/microscope inVia(Renishaw, UK) that was employed for measurements. The excitation laser used is 785 nm (NIR) source and grating period of 1200 lines/mm.

There are two main types of EM: 1) Scanning electron microscopy (SEM) and 2) Transmission Electron Microscopy (TEM). The main difference between these two techniques is that in SEM scattered electrons emitted from the surface of the specimen are detected while in TEM the electrons transmitted through the specimen are detected. Therefore, in order to study the surface of the structure, we perform SEM analysis.

3.2.1 Working principle of SEM imaging

The SEM consists of the following main components:
(i) An electron beam source (electron gun)
(ii) A vacuum chamber
(iii) A column consisting of condenser lens, scanning coil, objective lens, sample holder, detector.

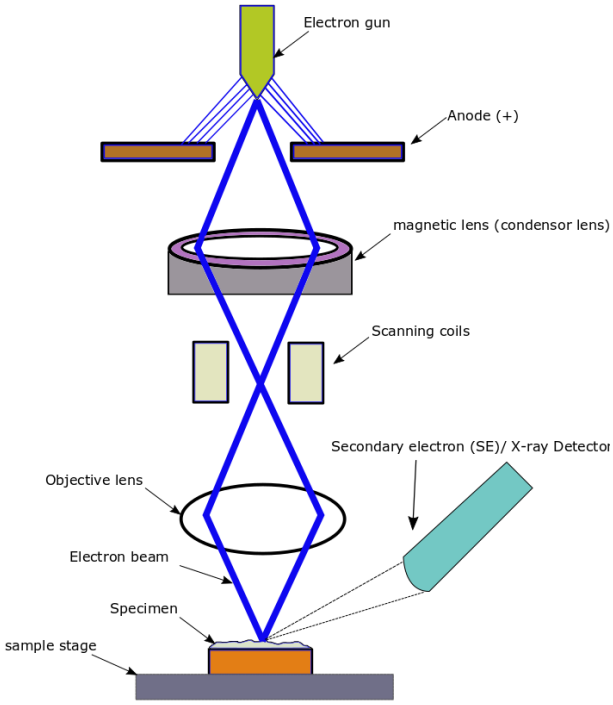

Figure 3.4: Schematic illustration for the working principle of Scanning electron microscopy (SEM). The signal collected by the detector is forwarded to the computer where the acquired signals are translated into an image

As shown in Fig. 3.4, the electron beam is generated by the electron gun within the vacuum chamber. These electrons pass through the electromagnetic field produced by the magnetic lens and are focused by the objective lens onto the specimen and are known as the primary electrons (PE). With the aid of scanning coils these electrons are scanned across the surface of the specimen in a raster pattern [50]. When the PE impinges on the specimen surface they generate signals due to the coulomb field interaction of the incoming electrons with that of the specimen and thus, generating secondary electrons (SE) or photons with wavelengths corresponding to that of X-Ray. Moreover, these signals are collected by the detector and from there onwards are processed by the computer.

3.2.2 Experimental details

SEM measurements were performed at Center for Physical Sciences and Technology (FTMC) Vilnius, Lithuania. The equipment used was Helios NanoLab 650 (FEI, Netherlands, 2011) with Schottky type field emission electron source was used to perform the imaging of surface with a resolution of 0.8 - 0.9 nm. The accelerating voltage of 3.00 kV and the cathode current was 25 pA at a tilt angle of 57°. For the samples with less surface charge density like the Graphene/SiO_2 and PyC/SiO_2, gold (Au) coating was performed in order to enhance the image quality, and prevent the overcharging on the surface.

3.3 Atomic force microscopy (AFM)

Atomic force microscopy is a high-resolution imaging technique that allows for exploring and obtaining measurement data for the samples at nano scale level. The AFM techniques involves a probe with a sharp tip which scans the sample back and forth to obtain the surface topography details. There are different scanning modes that enable the user to perform the characterization of electromagnetic and mechanical properties at the nanoscale.

3.3.1 Working principle of AFM

The schematic illustration of the working principle of an AFM is represented by Fig. 3.5 where it is shown that AFM employs a cantilever with a sharp tip and this assembly is often called the probe. The probe scans over the sample surface while the sample stage is moving in a raster scan motion. When the tip approaches the surface, the close-range attractive forces between the tip and the surface causes the cantilever to bend towards the surface. However, as the cantilever approaches the surface, the repulsive forces causes the cantilever to bend away from the surface. This up-down motion of the probe is detected by a laser beam that is reflected off the cantilever. The reflected beam is collected by the position sensitive photo detector that tracks and records those changes caused by the lateral and the vertical motion of the probe. The change in the position of the beam is converted into voltage in the detector from there onwards forwarded to the computer in a feedback loop which monitors and controls the height of tip above the surface. There are two major forms of AFM imaging: 1) Contact AFM ii) Non-contact AFM. Contact mode is

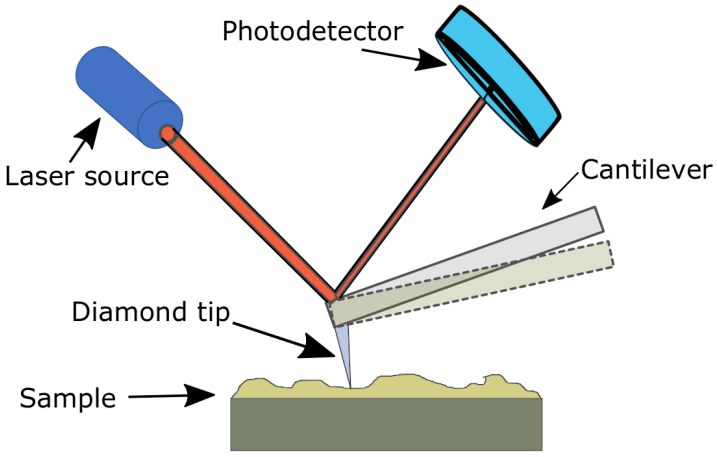

Figure 3.5: Working principle of Atomic force microscopy (AFM) in a tapping mode. The tip oscillates between the contacting sample surface. The variation in the sample surface is noted down by the photodetector due to variation in the position of the reflected laser beam collected by the photodetector.

most suitable for hard and stable samples and offers a better resolution and faster imaging. The disadvantage of this technique is that in this method the tip is always in contact with surface and it might cause damage to the sample surface. Therefore, this method is not suitable for thin films and rough surfaces. Whereas in the non-contact mode, the tip is oscillating just above the sample surface and is prevented to crash onto the surface by a feedback loop. Non-contact AFM preserves the sample surface. With sharper tips, higher quality imaging can obtained over prolong time.

3.3.2 Experimental details

The AFM measurements were performed at FTMC. The instrument used was BRUKER Dimension Icon AFM microscope as shown in Fig. 3.6 which is suitable for low-noise large area sample analysis. The sample was place on the stage as shown in Fig. 3.7. With the help of its custom software Nanoscope the measurement parameters were set as following:
Mode: Tapping mode, Scan size: 2 μm, Aspect ratio: 1, Scan rate (speed of tip movement): 0.300 Hz, samples per line: 512, Z-Scan range: 5 μm. For the measure-

ments, two different tips were used where each had different resonant frequencies and force constants. For the rougher surfaces like bSi+PyC and bSi Multi 75AI-G aluminum coated tip having resonant frequency of 75 kHz and force constant of 3 N/m was used. Whereas, for the smoother surface like PyC/SiO_2 and the Graphene on SiO_2, we used Tap300AI-G tip which has a higher force constant of 40 N/m and resonant frequency of 300kHz.

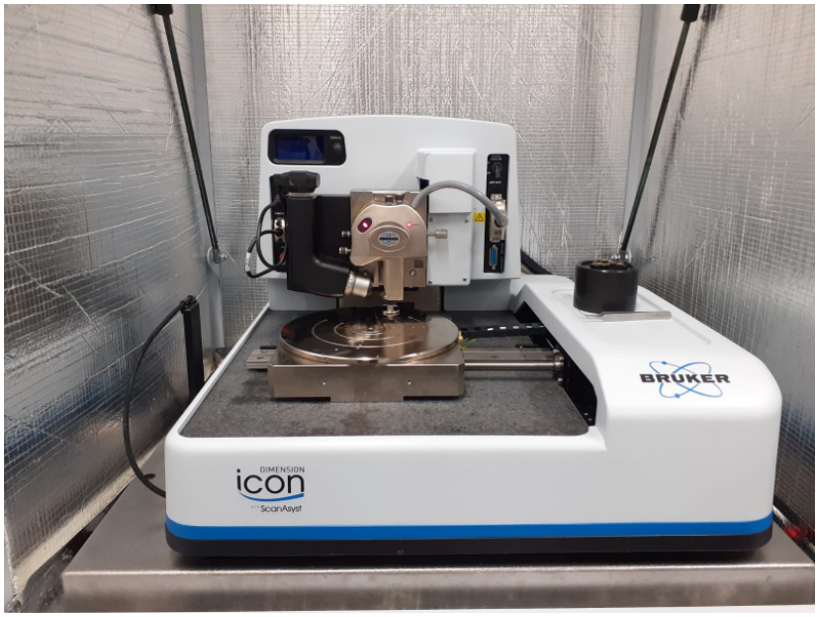

Figure 3.6: BRUKER Dimension Icon AFM microscope used for measuring the surface topography of the samples.

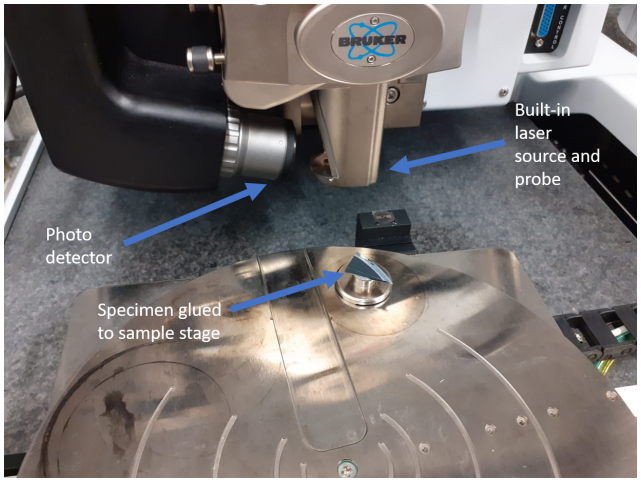

Figure 3.7: Closer view of the sample stage setup for AFM measurements. The laser beams are reflected by the cantilever and detected by the photodetector.

Chapter IV

Results and discussions

In this chapter we will discuss the results obtained from the CVD synthesized graphene on evaporated/sputtered Cu/Ni films on SiO_2 and PyC on bSi. Comparisons between different thicknesses of Cu films deposited on SiO_2 will be made. Furthermore, the difference in the quality of the obtained graphitic carbon will be discussed. The Black silicon coated with CVD synthesized PyC will also be studied and based on the results of Raman, AFM, SEM, spectroscopy the structural characterization of the samples will be performed.

4.1 Raman measurement

PyC/bSi, PyC/SiO_2 The Raman characterization results of the PyC (40 nm), PyC (20 nm), bSi(Aalto)+PyC and Graphene walls(285) can be seen in Fig. 4.1. For all the samples the G (graphitic) peak can be observed which indicates the presence of crystalline graphite. Disorder D peak can be also observed in each of the samples, and can be quantified by the I(D)/I(G) ratio which is higher for the PyC(40 nm)/SiO_2 than for the PyC(20 nm)/SiO_2. The fullwidth at half maximum (FWHM) and position of the G peak are also an important indicators of the degree of crystallinity and amorphization of graphitic carbon. The comparatively broader at 1595 cm^{-1} suggests that PyC(40 nm) thin film is a nanocrystalline graphite as also explained in [52]. The corresponding characteristic modes of these samples are summarized in the table 4.1 The absence of the 2D mode can be observed in all of the PyC samples which is in line with the general Raman spectra of PyC. There is red-shift of approximately 7 cm^{-1} observed between 40 nm and 20 nm PyC. This shift is due to the increase in the thickness of PyC which might have induced some

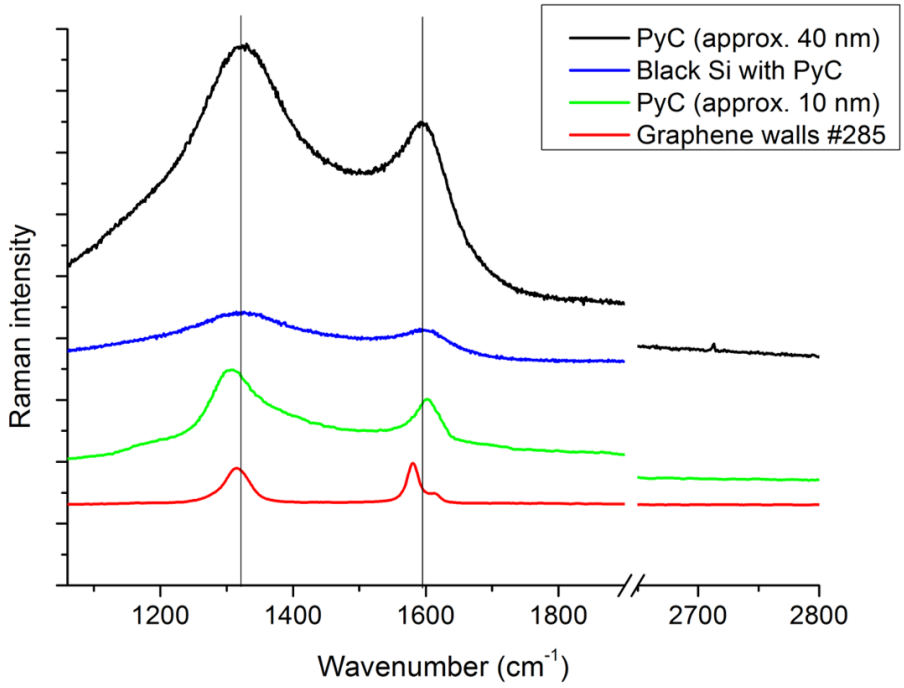

Figure 4.1: Raman spectra (λ = 785 nm of the fabricated samples: PyC(40 nm), PyC on Black Si, PyC (18 nm), Graphene walls(285).

stress/strain within the structure. Also, there is no shift in the G-mode observed in the sample PyC on SiO_2 and bSi. Which confirms that the shift is most probably due to the increased thickness.

Graphene on Cu/Ni SiO_2: In order to optimize the minimum possible sacrificial thickness of the Cu film, three different thickness of Cu films (50 nm, 200 nm, 400 nm) were thermally evaporated on SiO_2 substrate. Initially 50 nm Cu was considered for CVD graphene growth but with this thickness no graphitic carbon was observed with Raman measurements. Therefore, the thickness of Cu had to be significantly increased. Figure 4.2 represents the Raman spectra of CVD synthesized graphene on these three substrates. For all these samples measurements were performed with same excitation wavelength of 514 nm and 100 percent of the incident laser power. The details of the characteristic modes of both these samples are summarized in Table 4.2

TABLE 4.1

Raman measurement summary of the modes peak position of the samples.

Modes	PyC(40nm)	PyC(20nm)	bSi(Aalto)+PyC	Gr Wall (285)
G-Mode [cm^{-1}]	1595.2	1602.1	1595.2	1580.8
D-mode [cm^{-1}]	1322.6	1307.2	1322.2	1314.7

TABLE 4.2

Summary of the modes peak position of the graphene on thermally evaporated Cu samples.

Modes	Gr-Cu(200 nm)/SiO_2	Gr-Cu(400 nm)/SiO_2
G-Mode [cm^{-1}]	1593	1585
D-mode [cm^{-1}]	1322.6	1307.2
2D band [cm^{-1}]	2716	2695
FWHM(2D) [cm^{-1}]	30	34
I(2D)/I(G)	1.66	1.25

One can see from Fig. 4.2 that for the Cu film of thickness 50 nm no graphene was formed. This is due to the fact that Cu/SiO_2 system is stable at temperatures less 800 °C and at higher temperature it becomes unstable and evaporates. This is also mentioned in [43] where it is explained that the vapour pressure of Cu is 6 x 10^{-5} and the CVD was carried out at 1000 °C which is close to melting point of Cu i.e. 1084 °C therefore, such high temperature could have assisted the sublimation of Cu during growth process, thus hindering the graphene growth. As seen from Fig. 4.3(a), some bright random spot areas are observed. This could be due to the fact that during the CVD process the Cu layer has undergone dewetting and evaporation process which has caused morphological changes in the Cu film as also explained in [33] where both the Cu films (200 nm and 400 nm) high quality graphene is produced. Furthermore, in Fig. 4.2 the absence of the disorder D peak shows that it is a pristine graphene as in order for D peak to be excited, there must be a defect in the structure. Number of the graphene layers can be derived from the I(2D)/I(G) along with the FWHM of 2D peak. I(2D)/I(G) ratio for both 200 nm and 400 nm

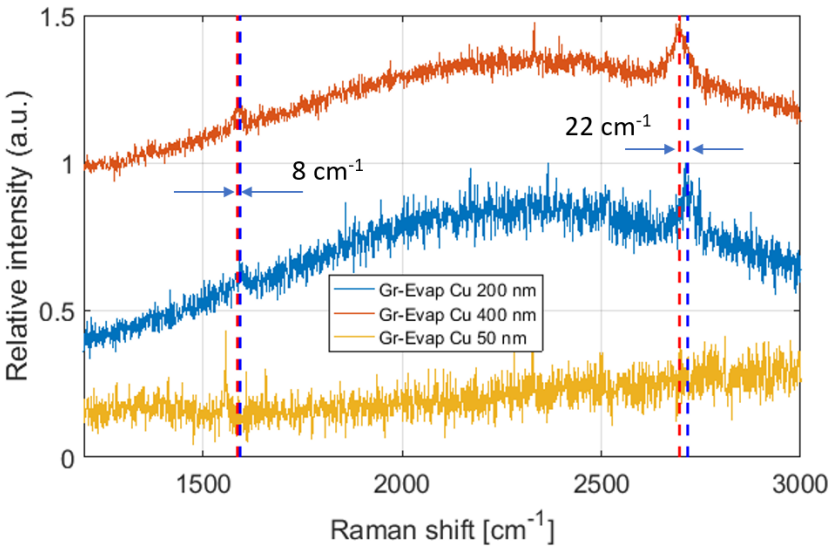

Figure 4.2: Raman spectroscopy with 514 nm laser. CVD grown graphene on thermally evaporated Cu films on SiO_2 substrate: Cu 50 nm (yellow), Cu 200 nm (blue) and Cu 400 nm (red).

Cu thicknesses is 1.66 and 1.25, respectively . Furthermore, the 2D FWHM is 30 and 34 cm^{-1} for each of the samples which confirms that it is a monolayer graphene. The 2D-peak and the G-peak are red-shifted by 21 cm^{-1} and 8 cm^{-1}, respectively. This shift could be possibly due to the charge doping or the induced stress as a result of lattice mismatch at sample/substrate interface. However, in [53] the possibility of only due to doping is ruled out as the 21 cm^{-1} red shift of 2D band is too large to be achieved by charge doping alone. Therefore, there is definitely some contribution due to stress. Similar redshift behavior is also observed in [54] where it is attributed due to the increase in the graphene layers (from SLG to FLG). Moreover, there is also increase in the FWHM of 2D band from 30 cm^{-1} to 34 cm^{-1} from 200 nm to 400 nm Cu thickness, respectively. The thickness of Cu film play a vital role in the formation of high quality graphene. In [55] it is mentioned that very thick films of Cu can cause strain in the resulting graphene structures. This can be seen by shift in G and 2D spectra as the thickness of Cu film is increased. Furthermore, in same work it is also mentioned that good quality graphene can be obtained between 500

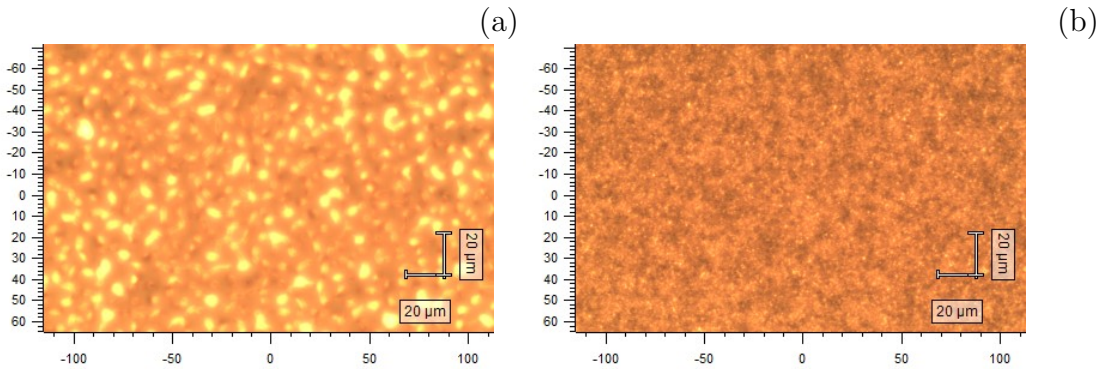

Figure 4.3: Optical microscopic image at x20 magnification showing the morphology of (a) 400 nm Cu and (b) 43 nm of Ni both on SiO_2 after the CVD Process.

nm - 800 nm Cu films however, in our experiment we were able to obtain pristine graphene at optimal Cu thickness of 400 nm.

Looking at Fig. 4.4, we observe that for the different thickness of Ni 30 nm and 43 nm which were prepared by the magnetron sputtering and thermal evaporation, respectively has resulted in graphene layers. The well defined 2D peak suggests the presence of graphitic carbon. The I(2D)/I(G) ratios confirm that these structures are not monolayered. The greater number of layers of graphene is due to the high solubility of carbon atoms in Ni which during the CVD annealing stage dissolute into Ni bulk and then precipitate out during cooling stage, thus resulting in multilayered graphene growth. However, in comparison to evaporated/sputtered Cu films on SiO_2 these much thin Ni films deposited on SiO_2 in similar technique have successfully resulted in graphene growth. This could be due to the difference in the melting point of Cu and Ni. Cu evaporation is much more likely due to lower melting point of 1084 °C compared to Ni with 1453 °C. Therefore, during the deposition process the evaporation of the substrate material is competing with the deposition of new material. As a result, with Cu 50 nm thickness we were not able to see any graphene sheet which is not the case for Ni. Lower thickness of films can be used with Ni for the CVD synthesis of graphene. Moreover, by looking at Fig. 4.3(b) we can see the absence of high concentration spots due to dewetting that were present in the case

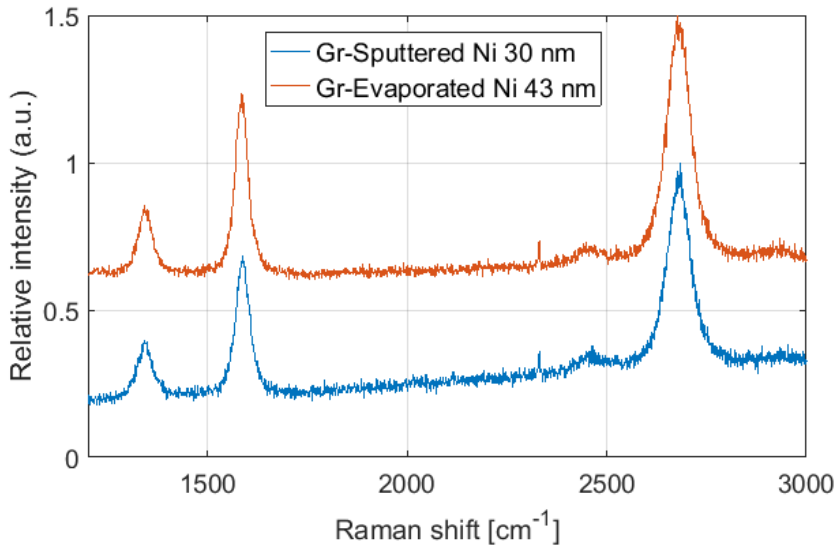

Figure 4.4: Raman spectra of Graphitic carbon CVD grown on thermally evaporated Cu film on SiO_2.

of Cu.

Graphene walls on Si (Gr-wall 285): As shown in the Fig. 4.1, the Graphene wall grown on Si have a distinct D and G peak at 1314.7 cm^{-1} and 1580 cm^{-1}, respectively. Moreover, there is also a D' peak (1612 cm^{-1}) observed near the shoulder of G peak. The presence of this peak signifies the increase in the amount of disorder in graphene. Shown in Fig. 4.5, the FWHM of 2D peak is 89 cm^{-1} approximately which further means there are higher orders of disorder fitted into the 2D peak. There are also D+D' (2424 cm^{-1}) and D+D" (2868 cm^{-1}) peaks observed in the neighborhood of 2D band. The emergence of these disorder peaks can be attributed to the electron beam exposure or the plasma etching during the fabrication steps that may have resulted in induced artificial defects in graphene. The ionized oxygen plasma that was generated during the plasma etching had an etching effect on graphene that resulted in defects. This fact is supported in [20], where a pristine graphene was exposed to electron beam dosage. The increase in the successive pulse dosage of plasma resulted in the emergence of D', D+D', D+D" peaks and the decrease in I(2D)/I(G) peak. The calculated I(2D)/I(G) ratio is 0.416.

The decrease in this ratio is mainly due to the defect induced suppression of the 2D lattice vibration , which is also mentioned in the same article.

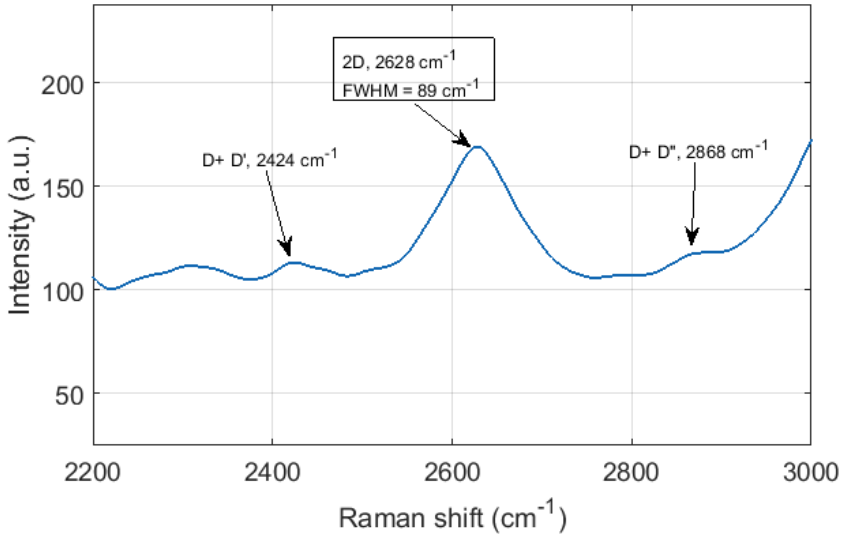

Figure 4.5: 2D centered Raman spectra of vertical graphene walls (285) grown on Si substrate measured at 785 nm wavelength laser.

4.2 SEM image Analysis

PyC on bSi, PyC on SiO_2: The SEM images of the PyC on SiO_2 for 20 nm and 40 nm thicknesses can be seen in Fig. 4.6. The images give us the topological details of the synthesized PyC directly on SiO_2 without presence of photo-resist. In Fig. 4.6(a,b) a thick film that is homogeneous and having grainy structure can be seen. On the other hand the PyC (20 nm) has grown uniformly throughout the substrate as can be seen in Fig. 4.6(d). Figure. 4.6(c) shows us the interface between the PyC and underneath SiO_2 substrate. The darker region shows us the PyC layer.

For the purpose of formation of ultra-thin film of PyC on Si, approximately 20 nm of PyC was CVD grown on bare Si substrate, the details of the synthesis can be found in the chapter 2 related to graphene and PyC synthesis. In the Fig. 4.7(a) bSi surface without the PyC coating can be seen. The structure consists of pyramid

like randomly distributed peaks. In Fig. 4.7(b) we can see the bSi coated with PyC layer. The structural morphology has been preserved however, with careful observation, it can be seen that the nano-scale roughnesses has been removed over the pyramids and has resulted in a much smoother surface. Comparison between different types of bSi (bSi(Aalto) and bSi(UEF)) substrates have also been made. Figure. 4.8 shows these two types of bSi. Firstly, the side view of the bSi(UEF) in Fig.4.8(a) has a much more rougher surface than the one in Fig. 4.8(c). Further it shows that these needles have further microscopic roughness in greater amount than in bSi(Aalto). Moreover, from Fig. 4.8(c) it can be observed that the density of the peaks is much greater for the bSi(Aalto) than that of the bSi(UEF). The Fig. 4.8(b) shows the top view of bSi(UEF) and it can be clearly seen that in the there are much greater voids in between the Si needles. Whereas, in Fig. 4.8(c) it shows that bSi(Aalto) has much more closely packed Si pyramids giving a smoother surface.

Graphene on Cu/Ni dielectric substrate: The thermally evaporated Cu film deposited onto SiO_2 substrate resulted in the formation of graphene structures. Figure. 4.9 shows the resulting morphology of the 400 nm copper film after CVD process. As discussed before the high temperature has resulted in evaporation and dewetting of the Cu film during the annealing stages. Finger-link Cu structures can be seen where the darker areas represent the graphene films, as shown in Fig. 4.9(b). Similar structures are also observed in [33], where the annealing temperature effects on the dewetting/evaporation of Cu films are discussed in detail. Similarly, by looking at Fig. 4.10(a), it is observed that contrary to the case of Cu, no such dewetting can be seen which would result in islands of Ni. The coating is smoother and different shades of gray can be seen. In fig. 4.10(b), the dark spots represent the grain surface of the Ni films. As also mentioned in [56], these dark areas are the hot-spots that contribute in the pumping of the carbon atoms out onto the Ni film surface and allowing it to spread through the surface. As a result, we obtain multi-layered graphene near these dark spots and single-bilayer graphene further away on Ni film which can be confirmed in Fig. 4.10(c) where different shades of gray layers shows the existence of multiple layers of graphene.

4.3 AFM surface roughness study

The summary of the macroscopic and microscopic roughness for the PyC samples and bSi with and without PyC can be found in the table. 4.3. The description of the AFM parameters mentioned in the table are as follow:
Surface Area (S.A) Difference – Difference between the image's three-dimensional Surface area and two dimensional projected surface area.
Image Rq – Root mean square average of height deviations taken from the mean image data plane.
Image Rmax – Maximum vertical distance between the highest and lowest data points in the image following the planefit.

PyC on bSi, PyC on SiO_2: In order to study the macroscopic and microscopic roughness of the samples as well as the topographical characterization, AFM image analysis was performed. The difference between the surface of PyC (20 nm)

Table 4.3

Summary of the AFM measurements to study the macroscopic and microscopic roughness of PyC (20 nm), PyC (40 nm), black Si, black Si with PyC

	PyC(20nm)	PyC(40nm)	bSi(Aalto)	bSi(Aalto)+PyC	bSi(UEF)
Image S.A diff [%]	0.444	2.21	134	135	233
Image R_q [nm]	0.847	2.49	77.1	70.6	177
Image R_{max} [nm]	12.3	36.7	495	509	144

and PyC (40 nm) can be observed from Fig. 4.11. As mentioned in Table.4.3, it can be seen that the PyC (20 nm), with R_q value of 0.847, has a much smoother surface with some thread-like structures compared to the PyC (40 nm) which has R_q value of 2.49 which is approximately 3 times that of PyC (20 nm) and thus have a rougher topography (see Fig. 4.11(c)). The PyC (40 nm) as shown in Fig.4.11(d) is much denser, while, the PyC (20 nm) has very scarce peaks with higher amplitudes as can be seen in Fig.4.11(b).

The AFM images in Figure. 4.12 represent bSi with and without PyC coating. By closely examining, we observe the thick pyramid like structure of bSi. From table 4.3, we determine the nanoscopic roughness of the bSi substrate before and

after the PyC coating, which is 77.1 nm and 70.6 nm, respectively. The decrease in the surface roughness can be well explained by the approx. 20 nm of PyC coating that has led to the nanoscale roughness of the bSi pyramids to be smoothed out. Moreover, the R_{max}, which is the difference between the maximum and minimum points of the AFM has also increased for bSi with PyC by 14 nm which confirms the deposition of PyC on the bSi substrate.

TABLE 4.4

Macroscopic and microscopic roughness of graphene deposited on evaporated Cu and Ni of 400 nm and 43 nm, respectively

	Cu (400 nm)	Ni (43 nm)
Image S.A diff [%]	8.07	11.2
Image R_q [nm]	293	75
Image R_{max} [nm]	1596	514

Graphene on Cu/Ni dielectric substrate: As seen from Fig. 4.13(a) the Cu film has undergone huge amount of dewetting during the annealing stage of CVD process which has set up islands of Cu with great heights. This is shown by the values in Table 4.4 where the R_{max} values for Cu(400 nm) and Ni (43 nm) are 1596 nm and 514 nm, respectively. Such great difference is accounted to the magnitude of dewetting which is considerably less for Ni, shown in Fig. 4.13(c)(d), due to its higher melting point and that has undergone the same CVD temperature conditions as Cu. The nano scale surface variations given by R_q value is also approximately 4 times greater for Cu than Ni.

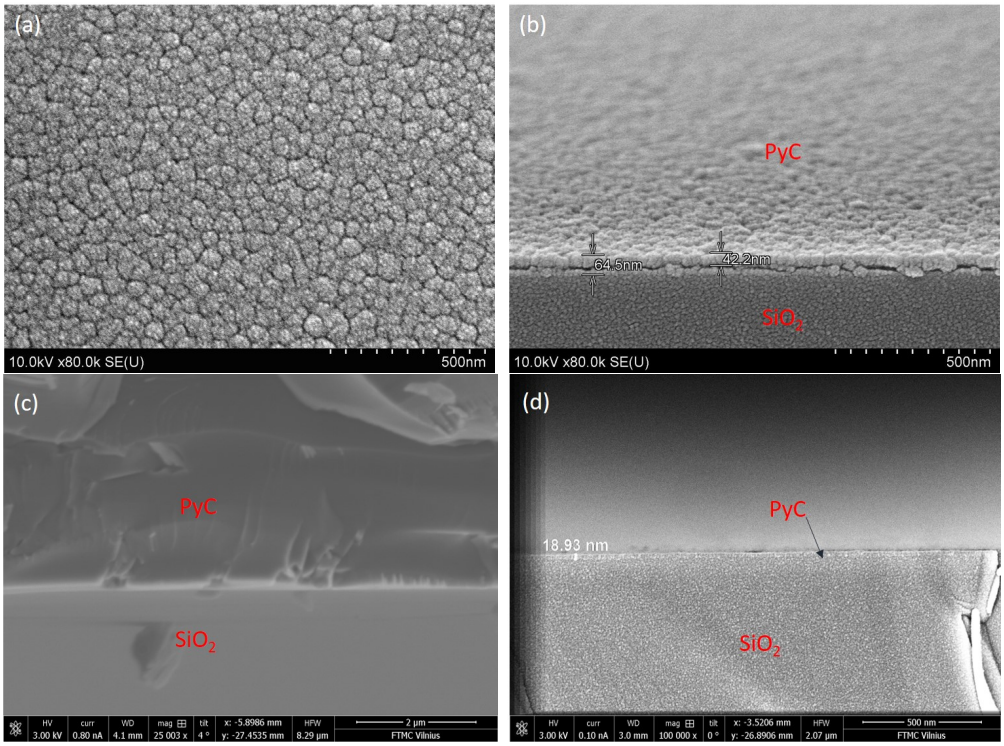

Figure 4.6: SEM surface images of the PyC/SiO_2 samples: (a) Top view image of PyC(40 nm) at x80000 magnification (b) Side view image of PyC(40 nm) at a tilt angle 4 degrees of and x25000 magnification (c) Top view image of PyC(20 nm) at x80000 magnification (d) Side view image of PyC(20 nm) at x100000 magnification. The images (b) and(d) show the deposited PyC layer with thickness of approximately 40 nm and 20 nm, respectively. Images (a),(b) and (d) are at a scale of 500 nm whereas, image (c) is at scale of 2 μm.

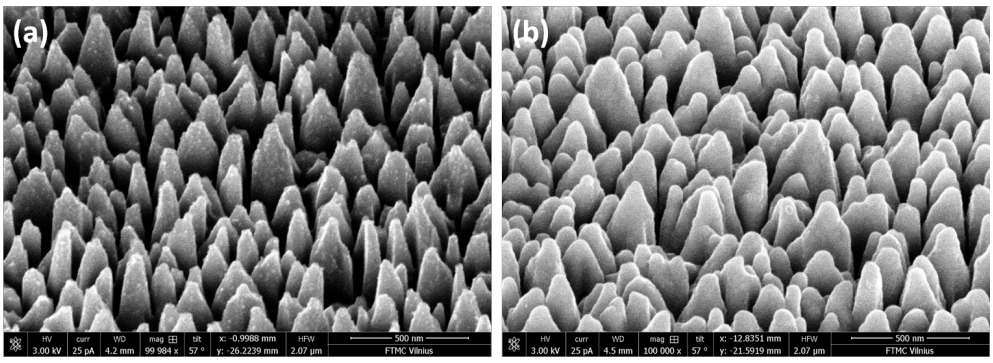

Figure 4.7: SEM surface images of bSi(Aalto) before and after PyC film deposition: (a) bSi(Aalto) before PyC deposition (b) bSi(Aalto) after deposition of approximately 20 nm PyC film. The images are taken at a scale of 500 nm with x100000 magnification and a tilt angle of 57 degrees. The bSi substrate consists of pyramid like silicon structures that are randomly distributed. The conformal PyC coating has resulted in the smoothening of the sharp roughness on these pyramids as can be observed in (b).

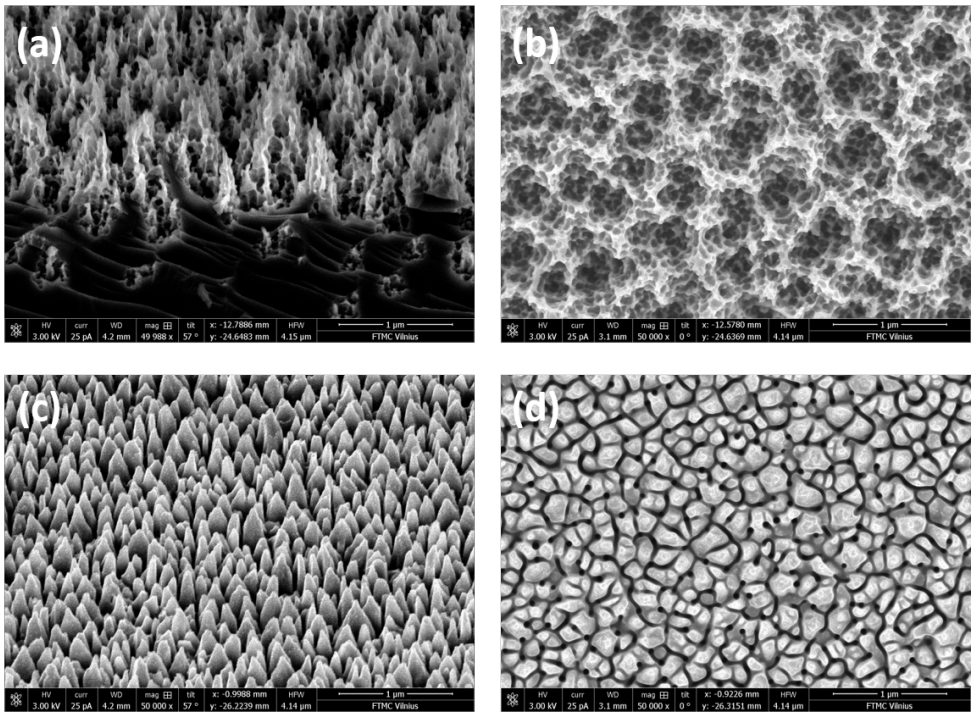

Figure 4.8: SEM surface images of two different types of bSi samples: (a)(b) represents the side view and top view of the bSi(UEF), respectively. (c)(d) represents the side and top view of the bSi(Aalto), respectively. All the images are taken at the same scale of 1 μm and x50000 magnification for comparison. Large void areas can be observed between the Si pyramids in case of bSi(UEF).

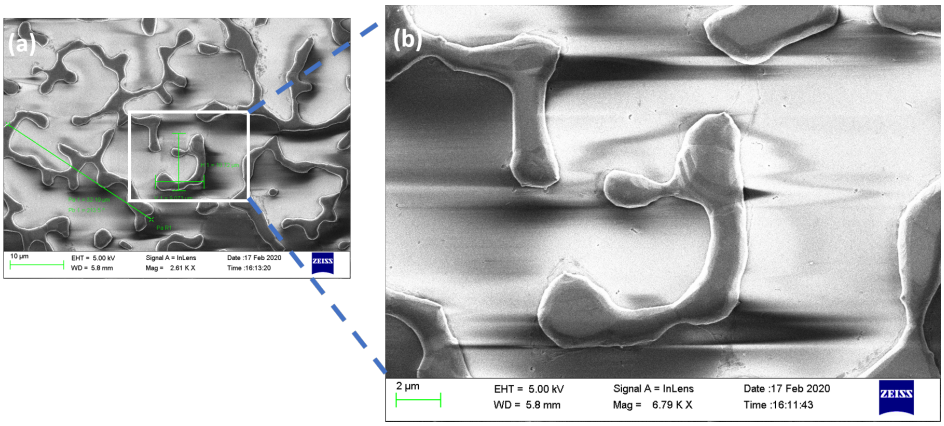

Figure 4.9: SEM surface images of thermally evaporated Cu film (400 nm) on SiO_2 substrate: (a) Shows the resulting dewetted Cu film after the CVD process (b) magnified image showing the darker area is graphene formed on the figure-like Cu structures.

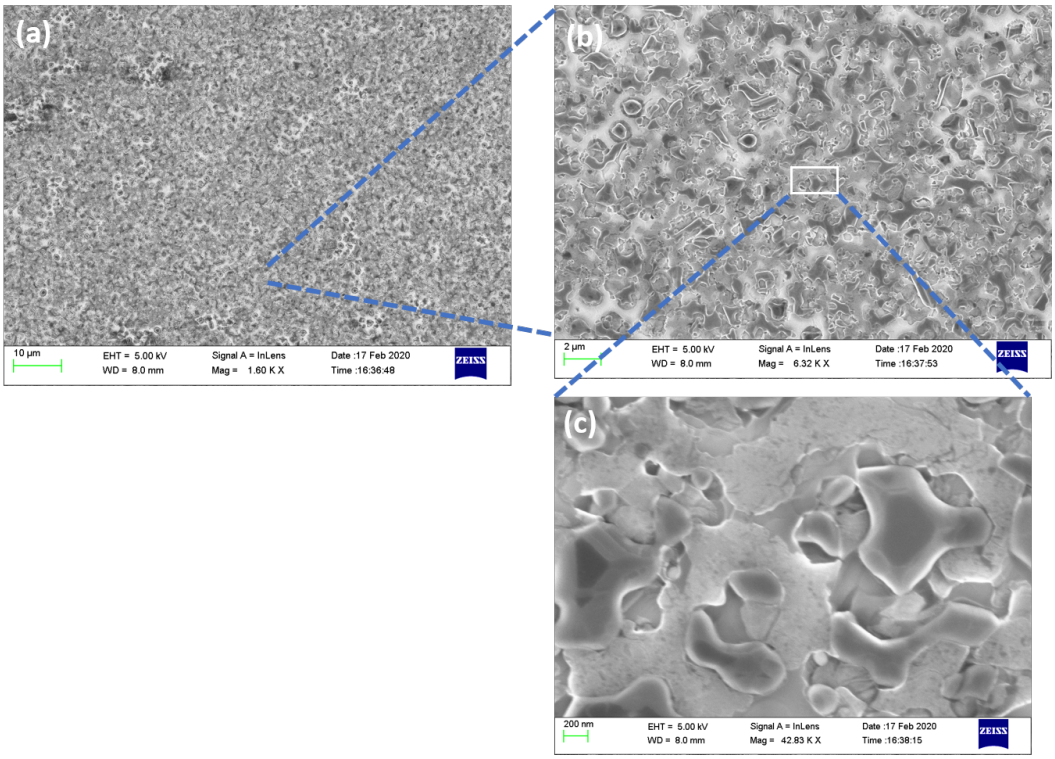

Figure 4.10: SEM surface images of thermally evaporated Ni film (43 nm) on SiO_2 substrate: (a) Shows the resulting morphology of the Ni film after the CVD process (b) magnified image showing the dark contrast areas as the Ni grain surface for carbon segregation (c) zoomed image The shades of dark regions represent multi-layered graphene structures.

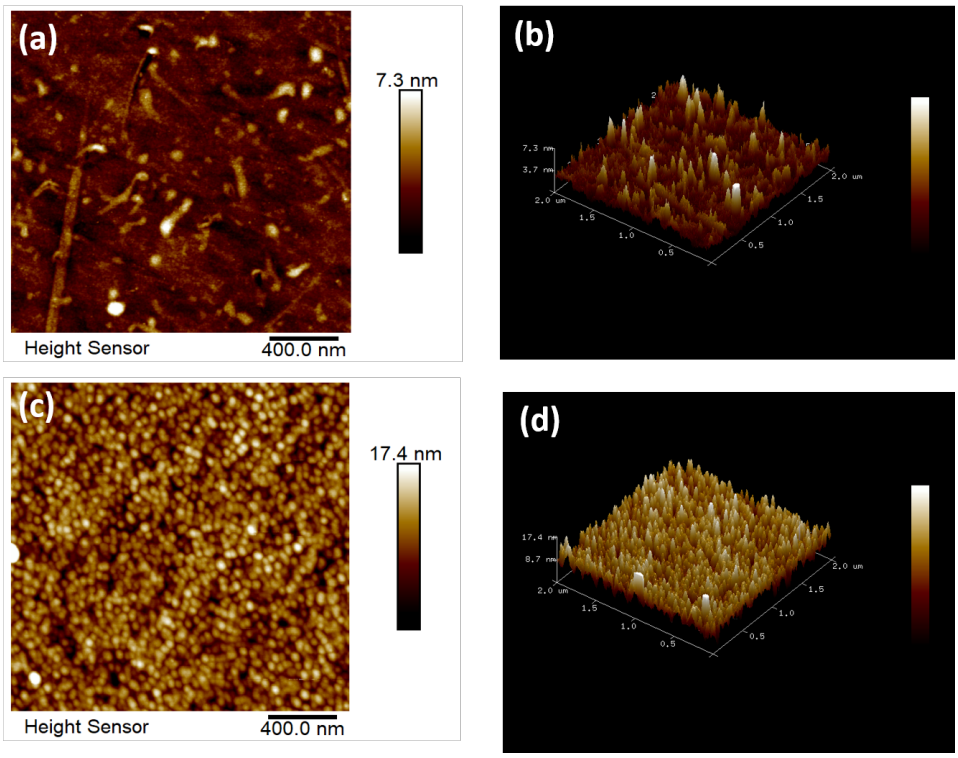

Figure 4.11: 2D and 3D AFM images of (a)(b) PyC 20 nm and (c)(d) PyC 40 nm. The scan size area for both the images is 10 μm x 10 μm and a scan rate of 0.403 Hz.

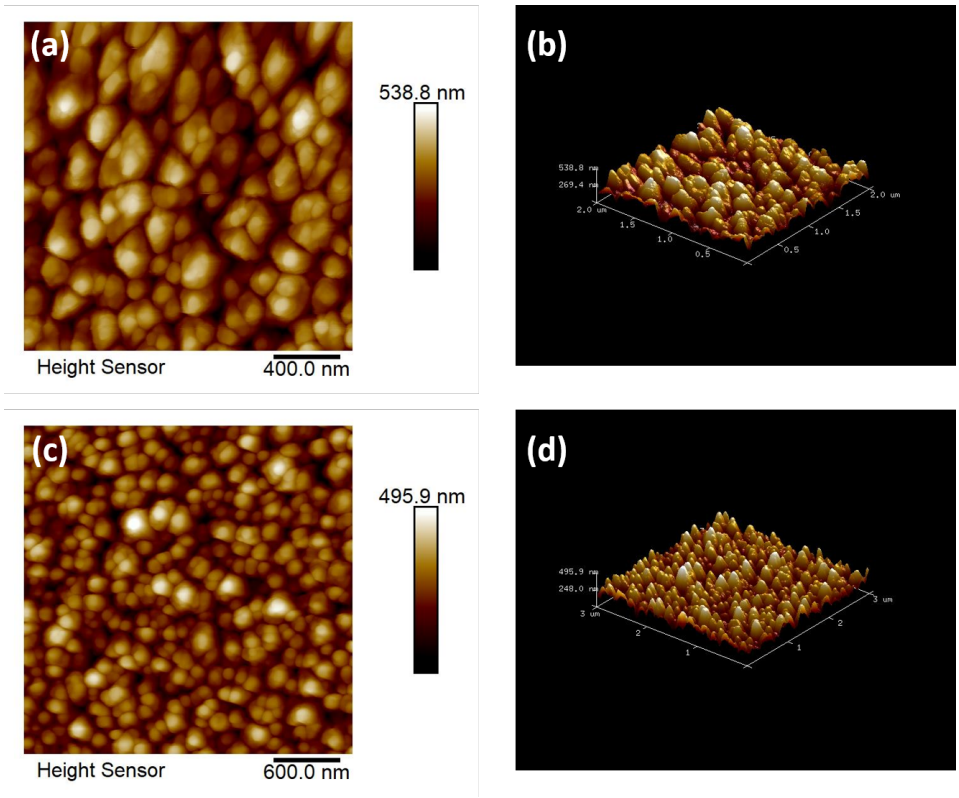

Figure 4.12: 2D and 3D AFM images of bSi(Aalto): (a)(b) bSi(Aalto) before the PyC film. The scanning field is 2 μm x 2 μm, (c)(d) bSi(Aalto) with approximately 20 nm PyC thin film coating. Scanning field of 3 μm x 3 μm and scanning rate 0.798 Hz.

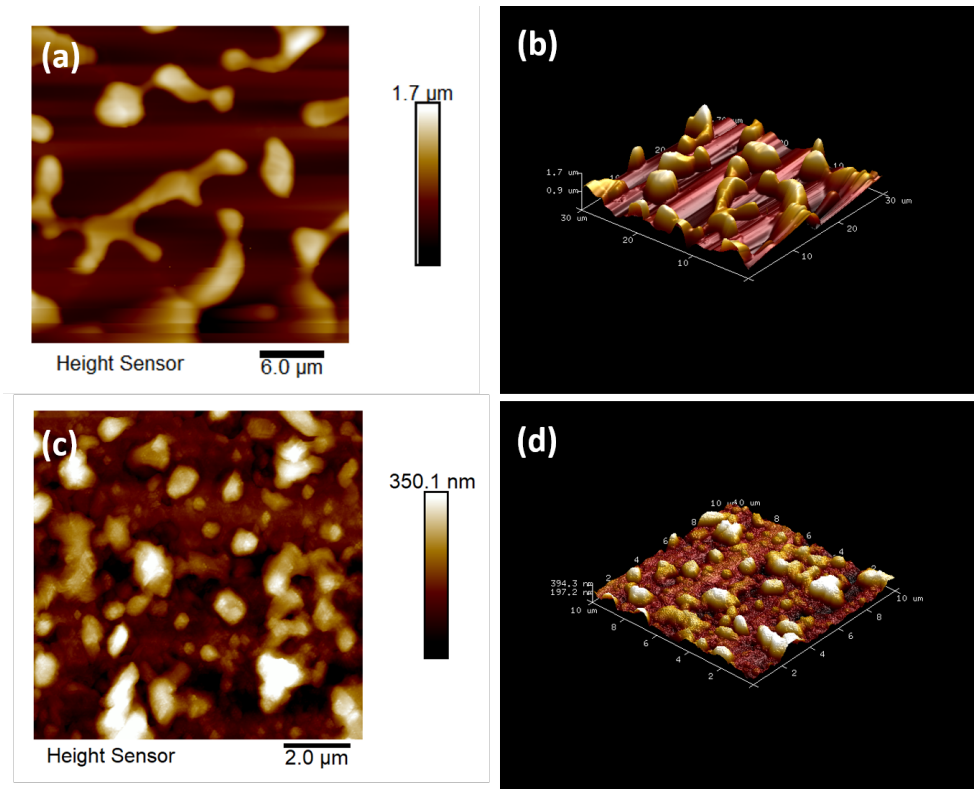

Figure 4.13: 2D and 3D AFM images of (a)(b) graphene through thermally evaporated Cu(400 nm) on SiO_2. Scanning field: 2 μm x 2 μm, scanning rate: 0.992 Hz. (c)(d) graphene through evaporated Ni(43 nm) on SiO_2. Scanning field: 2 μm x 2 μm, scanning rate: 0.401 Hz.

Chapter V

Bio-compatibility test

In this chapter we will focus on the procedure adopted to perform the biocompatibility test. The details for culturing the cell onto different substrate are highlighted. Moreover, the cell behavior and growth will be also analyzed. The possible effects of these substrates on the cell growth will also be discussed.

5.1 Cell culture

As a brain cells model we used rat glioma cells C6. ATCC C6 (ATCC ® CCL-107 ™) rat glioma cells, obtained from ATCC, LGC Standards, Ogrodowa 27/29, Kielpin, Poland, and were used throughout all experiments. Cells were grown in DMEM/F12 medium (Gibco) supplemented with 10% fetal bovine serum (Sigma) and 80 μg/mL gentamycin sulfate (Belmedpreparaty, Belarus) in 100% humidity at 37 °C in 5 % CO_2 atmosphere. In the log-phase cells were trypsinized, centrifuged, and 105 cells were seeded in standard 3.5 cm plastic petri dishes onto investigated substrates (bSi of 2 types: bSi(Aalto) and bSi(UEF)), bSi(Aalto)+PyC, PyC/SiO_2(2 types: 20 nm, 40 nm), graphene walls on Si) placed on the Petri dish bottom. Cells were cultured for 3 days. Growth medium components during measurements were replaced by Hepes buffer solution (pH 7.2) of the following content (in mmol/L): NaCl = 131, KCl = 5, MgSO = 4 - 1.3, CaCl = 2 – 1.3, Hepes = 20, $C_6H_{12}O$ = 6 – 5.

5.2 Fluorescent microscopy

Cells visualization was performed using DNA staining fluorescent dye propidium iodide. Before measurements substrates with cells on them were washed twice with Hepes buffer solution, fixed with ice-cold methanol for 30 minutes at 40 °C. Then substrates with cells were washed twice in Hepes buffer solution for 10 minutes each time and once with deionized water. During the measurements water was replaced with 10-6 mol/L propidium iodide solution. Excitation wavelength was 532 nm, emission maximum was 617 nm. Laser intensity before the ND filter wheel was 10.7 mW.

5.3 Cells interaction with bio-substrate

The microscopic images obtained of cells that were fixed onto different substrates were analyzed using the ImageJ which is an image processing and analysis software. For the analysis we count the number of cells in a 512 μm x 512 μm area of interest and also calculate the total relative area that is occupied by the cells. Figure. 5.1 represents the control group where cells are fixed onto a plastic petri dish.

In Fig. 5.2 comparison of the projected area covered by the cells is made between bSi(Aalto) and bSi(Aalto)+PyC(approx. 20 nm thickness). Clearly it can be seen that with PyC coating the cell has not been able to grow its processes and thus shows the lack of affinity of the cells to the PyC surface. The result mentioned in Table 5.1 shows that the bSi(Aalto) has average %relative area coverage of 16.15% compared to that of bSi(Aalto)+PyC having 7.01% area coverage. This dramatic reduction in the cell growth and expansion can be explained by the AFM roughness results mentioned in Table 4.3 where there the R_q value has reduced from 77.1 to 70.6 after bSi(Aalto) was covered with PyC film. Even though the macroscopic morphology is preserved but there has been reduction in the nanoscopic roughness as it is clearly visible in Fig. 4.7. In order to draw comparison to the bSi(Aalto), the cell growth on the bSi(UEF) can be seen in Fig. 5.3, where it can be observed that the even though there are not many cells but still they have formed colonies. The cells are struggling to find the contact surface and that is why elongated processes can be observed. This could be due to the fact that as seen in Fig. 4.8(b), there are large gaps between the Si needles in bSi(UEF) compared to that of bSi(Aalto) where needles are packed more closely together, as shown in Fig. 4.8(d). Furthermore, also from the table

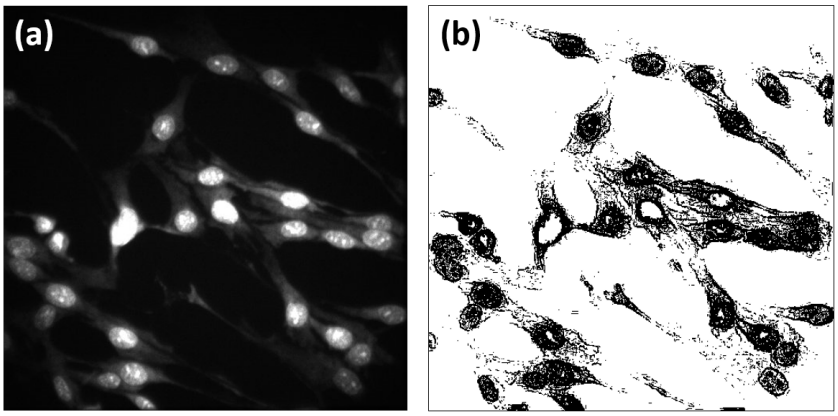

Figure 5.1: (a) Fluorescent microscope image of ATCC ® CCL-107 ™ rat glyoma cells fixed with ice cold methanol stained with 1E-6 M propydium iodide in Hepes buffer (pH 7.2) on the bottom of a plastic petri dish for visualization. (b) The resulting after image processing and thresholding for calculating the relative area covered by the cells and the cell count within the area of interest.

5.1 we can see that the relative coverage area of bSi(UEF) is 7.41% which is higher than that of bSi(Aalto)+PyC with 7.01% but lower than that of bSi(Aalto) with 16.15%. This is explained well by the possibility that cells are not able to detect the surface contact in bSi(UEF) due to these large distances in between nearby needles. In addition, another possibility could be the extremely large surface roughness of 177 nm of bSi(UEF), which is more than twice for that of PyC(Aalto).

Figure. 5.4 shows a comparison between two different thicknesses of PyC (20 nm and 40 nm) on a flat quartz substrate. For the PyC(20nm) it is shown in Fig.5.4(a) in the encircled portion that the processes of the cells are elongated. This is due to absence of the the macro and micro scale roughness. The cells cannot find a nearby contact and instead join processes with their neighboring cells thus, forming their own network. The PyC(40nm) in Fig.5.4(b) shows better results, the cells even though don't have good contact with the surface they are not able to spread. These neuron cells are preferring to establish contacts among themselves.

Furthermore, in Fig. 5.5 the cell growth Si substrate covered with vertical graphene walls can be seen. The cells growth is observed to be staggered. In-

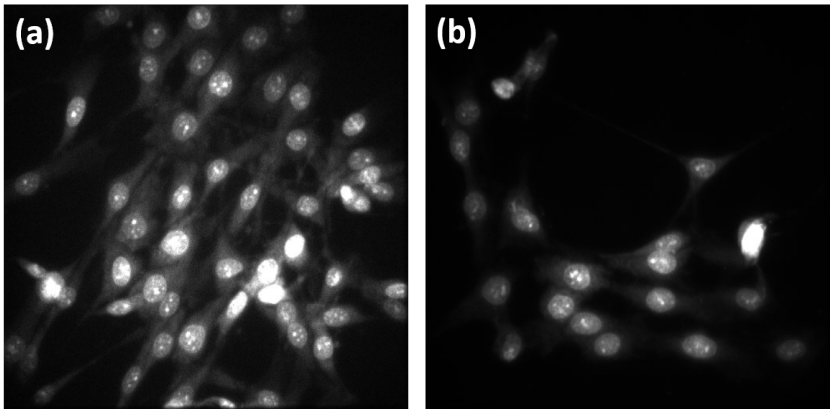

Figure 5.2: Glioma cell growth on (a) bSi(Aalto) without PyC thin film and (b) bSi(Aalto) with approx. 20 nm PyC coating.

stead of attaching to the surface, cells are forming contacts among themselves as highlighted by the red circle. The lack of affinity with the substrate could be due the hydrophobic nature of these graphene nanostructures. This sample has the value of around 3.83% relative area coverage which is the least compared to PyC and bSi samples.

Table 5.1

Biocompatibility test analysis of the cells fixed onto different substrates. The relative %area coverage by the cells in a 512 μm x 512 μm area of interest is summarized in the table.

	Plastic	PyC(20nm)	bSi(Aalto)	bSi(Aalto)+PyC	bSi(UEF)	Gr wall-285
%Area	17.06	11.526	16.15	7.01	7.41	3.83
cells	15	14.8	36.25	12.7	12.14	6.714
%Area/Cell	1.13	0.8128	0.4455	0.551	0.6103	0.5700

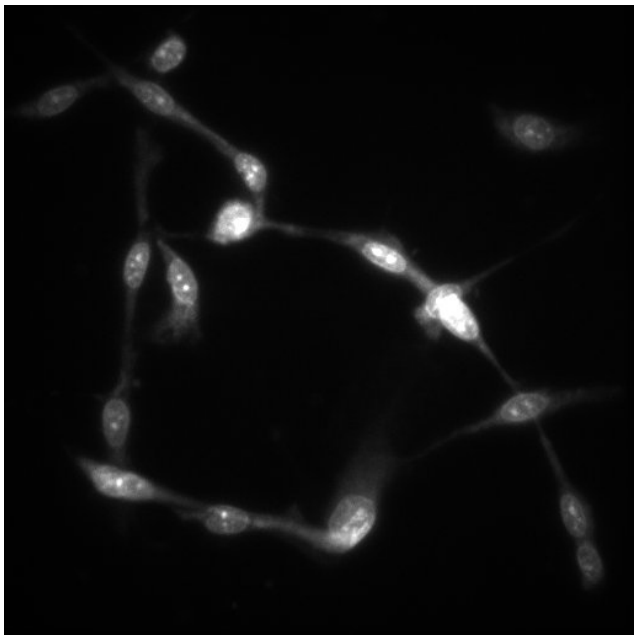

Figure 5.3: Glioma cell growth on bSi(UEF). The cells are shown to form colonies and elongated processes suggesting the lack of contact surface.

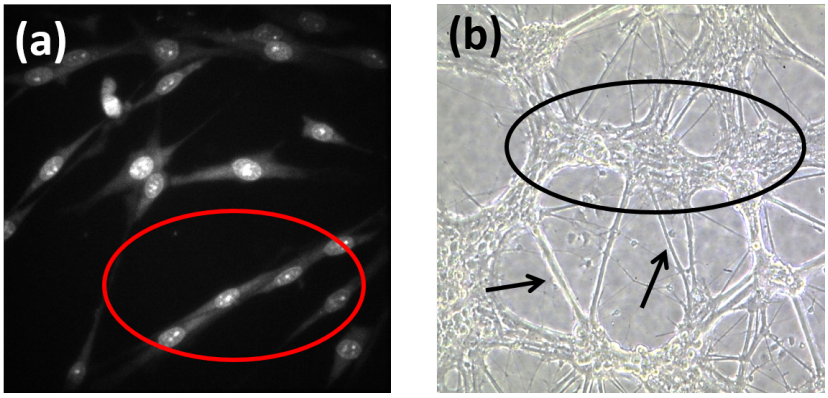

Figure 5.4: (a) Glioma cell growth on 20 nm PyC coated SiO_2 substrate (b) Neuron cells on PyC 40 nm. The red encircled cells depict elongation of the cell processes due to the lack of surface contact.

Figure 5.5: Glioma cell growth on graphene walls (285).

Chapter VI

Conclusions

In our work we have focused on the study of carbon-based nanomaterials to develop bio-compatible substrates for the cells growth and sensing. For this purpose we synthesized/used different configuration of carbon based substrates such as PyC/SiO_2, bSi/PyC, graphene on Cu/Ni coated dielectric as well as vertical graphene walls on Si wafer.

For the intrinsic structural characterization Raman spectroscopy was performed on all the samples. The results as shown in Fig. 4.1 suggest the presence of G peak in all the samples which mean all of them had some form of graphitic carbon present. For the PyC and bSi with PyC there is no shift in the G and D peak but as the the thickness of PyC increased, a red shift of 6.9 cm^{-1} was observed thus, suggesting that increase in thickness causes a strain between the structure of PyC and the underneath quartz substrate. Similar behavior was also observed in case of graphene on Cu coated, with two different thicknesses (200 nm and 400 nm), on silica substrate. Therefore, the optimal thickness of the film is of utmost importance in order to avoid unnecessary strain in the substrate structure. Thus, there should be optimization of different parameters of the CVD process in order to obtain the desired thickness and roughness of the PyC and graphene structures.

Further investigation of Raman for graphene walls (285) revealed that during the fabrication excessive exposure to plasma etching has induced defects into the graphene structure which is represented by the D'(1612 cm^{-1}) peak. Therefore, the post-fabrication steps of graphene walls need to be optimized, for instance, reducing the number of exposure of plasma pulses in order to obtain high quality graphene with low defects.

From the SEM analysis, the image of the bSi(Aalto)+PyC shown in Fig. 4.7 suggests that the PyC coating has dramatically reduced the nanoscopic and microscopic roughness on the Pyramid structures of bSi(Aalto). Moreover, the depth of the needles (from the base to the tip) was also reduced after 20 nm of PyC film deposition. Therefore, the PyC coating provides the option of the tun-ability of the roughness of the bSi structure which in result can alter the surface charge properties of the bSi. Moreover, the bio-compatibility test revealed that the macro, micro and nano scale roughness plays a vital role in the cell adhesion and growth on the bio-substrate. The bSi has a combination of macroscopic and microscopic roughness with surface charge distribution, which promotes the cell anchorage and adhesion. However, this adhesion greatly reduced when coated with 20 nm of PyC. This effect may originate from shielding the surface charges of bSi by the PyC film. Furthermore, this coating has reduced its surface micro and nano scale roughness and resulted in decrease in the cell process adhesion. Almost the same amount of cell adhesion was also observed for PyC(20 nm) on a flat SiO_2 substrates, thereby excluding the macro and microscopic roughness. Therefore, it can be concluded that the success of cell adhesion is greatly influenced by the macroscopic surface roughness. The comparison between bSi(Aalto) and bSi(UEF) showed that the later, having more than twice the surface roughness than that of bSi(Aalto), had cells covering only 7.41% of the total area. Thus, it is imperative to have the optimal macroscopic roughness that promotes the cell contact with the surface as too large macroscopic roughness can also lead to difficulties in establishing of cell contact with the surface.

For the graphene study we considered two different configurations: graphene on Cu/Ni coated dielectric (SiO_2) and vertical graphene walls deposited on Si substrate. The Cu/Ni grown graphene substrates failed the biocompatibility test due to the challenges in completely etching of the metal film from in between graphene and dielectric substrate. Dewetting and evaporation of the Cu/Ni films for longer annealing duration during the CVD process is also an option that can be considered. The presence of these transition metals is not suitable for the cell growth due to their toxicity and therefore further optimization and careful procedures should be implemented in order to completely get rid of the metal layer underneath graphene.

Compared to PyC, with graphene walls the cells were struggling to attach to the surface and were not successful in growing their processes. In fact, the cells close to each other were able to make contacts with the neighboring cell. This

gives us information that the orientation of graphene plays a vital role in tuning the hydrophobicity and hydrophilicity nature of the final bio-substrate. Due to the nano-structured surface, graphene walls are super hydrophobic and therefore this can be used to achieve directed neuron growth.

The thorough study conducted on the development of carbon based nanomaterials deposited on various substrates and their configurations have given us insight into the importance of the surface morphology and topography of the bio-substrates and how variations even on the nano scale can immensely effect the bio-compatibility of the final scaffold. Therefore, it is imperative to take into consideration the parameters like roughness, thickness, surface charge distribution, hydrophilic/hydrophobic nature and orientation of the bio-substrates for the efficient cell adhesion and differentiation that will be a step forward in realization of *distributed sensor networks for living cells functional state monitoring*. The collected results will be the basis for the paper which is in progress. The manuscript "*Graphene multilayers as versatile platform for bio-photonics*" is ready for submission to ACS Appl Materials and interfaces. Furthermore, a poster presentation of the current work has been submitted to "Physics Days", University of Eastern Finland, Kuopio, April 2020.

References

[1] K. Batrakov, P. Kuzhir, S. Maksimenko, A. Paddubskaya, S. Voronovich, P. Lambin, T. Kaplas, and Y. Svirko, "Flexible transparent graphene/polymer multilayers for efficient electromagnetic field absorption," *Scientific reports* **4**, 7191 (2014).

[2] K. Batrakov, P. Kuzhir, S. Maksimenko, A. Paddubskaya, S. Voronovich, T. Kaplas, and Y. Svirko, "Enhanced Microwave Shielding Effectiveness of Ultrathin Pyrolytic Carbon Films," *Applied Physics Letters* **103** (2013).

[3] M. Baah, P. Obraztsov, A. Paddubskaya, A. Biciunas, S. Suvanto, Y. Svirko, P. Kuzhir, and T. Kaplas, "Electrical, Transport, and Optical Properties of Multifunctional Graphitic Films Synthesized on Dielectric Surfaces by Nickel Nanolayer-Assisted Pyrolysis," *ACS Applied Materials & Interfaces* **12**, 6226–6233 (2020).

[4] P. Mehrotra, "Biosensors and their applications – A review," *Journal of Oral Biology and Craniofacial Research* **6**, 153 – 159 (2016).

[5] R. Monošík, M. Streďanský, and E. Šturdík, "Biosensors - classification, characterization and new trends," *Acta Chimica Slovaca* **5** (2012).

[6] V. B. C. D. Farida Veliev, Anne Briançon-Marjollet, "Impact of crystalline quality on neuronal affinity of pristine graphene," *Biomaterials* **86**, 33–41 (2016).

[7] T. Z. Hong Zhou, Anju Gupta and J. Zhou, "Three-dimensional graphene foam as a biocompatible and conductive scaffold for neural stem cells," *International Journal of Molecular Sciences* **8**, 884–893 (2007).

[8] T. Limongi, F. Cesca, F. Gentile, R. Marotta, R. Ruffilli, A. Barberis, M. Dal Maschio, E. Petrini, S. Santoriello, F. Benfenati, and E. Di Fabrizio, "3D Cell Cultures: Nanostructured Superhydrophobic Substrates Trigger the Development of 3D Neuronal Networks (Small 3/2013)," *Small (Weinheim an der Bergstrasse, Germany)* **9** (2013).

[9] G. T. Teixidor, R. A. Gorkin, P. P. Tripathi, G. S. Bisht, M. Kulkarni, T. K. Maiti, T. K. Battacharyya, J. R. Subramaniam, A. Sharma, B. Y. Park, and M. Madou, "Carbon microelectromechanical systems as a substratum for cell growth," *Biomedical Materials* **3**, 034116 (2008).

[10] V. M. R. C. H. Hui Hu, Yingchun Ni and V. Parpura, "Chemicall Functionalized Carbon Nanotubes as Substrates for Neuronal Growth," *Nano Letters* **4**, 507–511 (2004).

[11] Q. Z. Y. T. X. L. M. Y. Ho Pan Bei, Yuhe Yang and X. Zhao, "Graphene-Based Nanocomposites for Neural Tissue Engineering," *Molecules* **24**, 658 (2019).

[12] F. Menaa, A. Abdelghani, and B. Menaa, "Graphene nanomaterials as biocompatible and conductive scaffolds for stem cells: impact for tissue engineering and regenerative medicine," *Journal of Tissue Engineering and Regenerative Medicine* **9**, 1321–1338 (2015).

[13] S. Ryu and B.-S. Kim, "Culture of Neural Cells and Stem Cells on Graphene," *Tissue Engineering and Regenerative Medicine* **10**, 39–46 (2013).

[14] D. Convertino, S. Luin, L. Marchetti, and C. Coletti, "Peripheral Neuron Survival and Outgrowth on Graphene," *Frontiers in Neuroscience* **12**, 1 (2018).

[15] q. Z. Ning Li and Q. Song, "Three-dimensional graphene foam as a biocompatible and conductive scaffold for neural stem cells," *Scientific Reports* **3**, 1604 (2013).

[16] Edwards and B. T, *Graphene: Mechanical Properties, Potential Applications and Electrochemical Performance* (Nova Science Inc, 2014).

[17] S. Cook, R. Beckenbaugh, J. Redondo, L. Popich, J. Klawitter, and R. Linscheid, "Long-Term Follow-up of Pyrolytic Carbon Metacarpophalangeal Implants," *The Journal of bone and joint surgery. American volume* **81**, 635–48 (1999).

[18] A. Shah, P. Stenberg, L. Karvonen, R. Ali, S. Honkanen, H. Lipsanen, N. Peyghambarian, M. Kuittinen, Y. Svirko, and T. Kaplas, "Pyrolytic carbon coated black silicon," *Scientific reports* **6**, 25922 (2016).

[19] G. Dovbeshko, V. Romanyuk, D. Pidgirnyi, V. Cherepanov, E. Andreev, V. Levin, P. Kuzhir, T. Kaplas, and Y. Svirko, "Optical Properties of Pyrolytic Carbon Films Versus Graphite and Graphene," *Nanoscale Research Letters* **10**, 234 (2015).

[20] I. Childres, L. Jauregui, W. Park, H. Caoa, and Y. Chena, "Raman Spectroscopy of Graphene and Related Materials," *New Developments in Photon and Materials Research* 403-418 (2013).

[21] A. Dubey, S. Dave, M. Lakhani, and A. Sharma, "Applications of graphene for communication, electronics and medical fields: A review," (2016), pp. 2435–2439.

[22] F. Schwierz, "Graphene transistors," *Nature nanotechnology* **5**, 487–96 (2010).

[23] V. Skakalova and A. B. Kaiser, *Graphene: Properties, Preparation, Characterisation and Devices*, 7th ed. (Woodhead Publishing, 2014).

[24] P. Avouris and C. Dimitrakopoulos, "Graphene: synthesis and applications," *Materials Today* **15**, 86 – 97 (2012).

[25] K. Novoselov, A. Geim, S. Morozov, D. Jiang, Y. Zhang, S. Dubonos, I. Grigorieva, and A. Firsov, "Electric Field Effect in Atomically Thin Carbon Films," *Nat. Mater.* **6** (2004).

[26] B. Min, D. W. Kim, K. Kim, H. Choi, S. Jang, and H.-T. Jung, "Bulk scale growth of CVD graphene on Ni nanowire foams for a highly dense and elastic 3D conducting electrode," *Carbon* **80**, 446–452 (2014).

[27] A. Graham, G. Schindler, G. Duesberg, T. Lutz, and W. Weber, "An investigation of the electrical properties of pyrolytic carbon in reduced dimensions: Vias and wires," *Journal of Applied Physics* **107**, 114316 – 114316 (2010).

[28] N. Mcevoy, N. Peltekis, S. Kumar, E. Rezvani, H. Nolan, G. Keeley, W. Blau, and G. Duesberg, "Synthesis and analysis of thin conducting pyrolytic carbon films," *Carbon* **50**, 1216–1226 (2012).

[29] Z. Sun, A. Martinez, and F. Wang, "Optical modulators with 2D layered materials," *Nature Photonics* **10**, 227–238 (2016).

[30] M. Liu, X. Yin, E. Ulin-Avila, B. Geng, T. Zentgraf, L. Ju, F. Wang, and X. Zhang, "A graphene-based broadband optical modulator," *Nature* **474**, 64—67 (2011).

[31] S. De and J. Coleman, "Are There Fundamental Limitations on the Sheet Resistance and Transmittance of Thin Graphene Films?," *ACS nano* **4**, 2713–20 (2010).

[32] A. B. Djurišić and E. H. Li, "Optical properties of graphite," *Journal of Applied Physics* **85**, 7404–7410 (1999).

[33] Y. Chen, G. Kang, A. Shah, V. Pale, Y. Tian, Z. Sun, I. Tittonen, S. Honkanen, and H. Lipsanen, "Improved SERS Intensity from Silver-Coated Black Silicon by Tuning Surface Plasmons," *Advanced Materials Interfaces* **1**, 1300008 (2014).

[34] A. Shah, *Black silicon technology and applications*, PhD thesis 2016).

[35] C.-M. Seah, S.-P. Chai, and A. R. Mohamed, "Mechanisms of graphene growth by chemical vapour deposition on transition metals," *Carbon* **70**, 1 – 21 (2014).

[36] K. Alshurman and H. H. Naseem, "CVD Graphene Growth Mechanism on Nickel Thin Films," (2014).

[37] B. Hu, H. Ago, C. M. Orofeo, Y. Ogawa, and M. Tsuji, "On the nucleation of graphene by chemical vapor deposition," *New J. Chem.* **36**, 73–77 (2012).

[38] A. Obraztsov, I. Pavlovsky, A. Volkov, A. Petrov, V. Petrov, E. Rakova, and V. Roddatis, "Electron field emission and structural properties of carbon chemically vapor-deposited films," *Diamond and Related Materials* **8**, 814 – 819 (1999).

[39] M. Losurdo, M. Giangregorio, P. Capezzuto, and G. Bruno, "Graphene CVD growth on copper and nickel: Role of hydrogen in kinetics and structure," *Physical chemistry chemical physics : PCCP* **13**, 20836–43 (2011).

[40] M. Regmi, M. F. Chisholm, and G. Eres, "The effect of growth parameters on the intrinsic properties of large-area single layer graphene grown by chemical vapor deposition on Cu," *Carbon* **50**, 134 – 141 (2012).

[41] N. S. Mueller, A. J. Morfa, D. Abou-Ras, V. Oddone, T. Ciuk, and M. Giersig, "Growing graphene on polycrystalline copper foils by ultra-high vacuum chemical vapor deposition," *Carbon* **78**, 347 – 355 (2014).

[42] L. Baraton, Z. B. He, C. S. Lee, C. S. Cojocaru, M. Châtelet, J.-L. Maurice, Y. H. Lee, and D. Pribat, "On the mechanisms of precipitation of graphene on nickel thin films," *EPL (Europhysics Letters)* **96**, 46003 (2011).

[43] Y. Zhang, L. Gomez, F. N. Ishikawa, A. Madaria, K. Ryu, C. Wang, A. Badmaev, and C. Zhou, "Comparison of Graphene Growth on Single-Crystalline and Polycrystalline Ni by Chemical Vapor Deposition," *The Journal of Physical Chemistry Letters* **1**, 3101–3107 (2010).

[44] A. C. Ferrari and J. Robertson, "Interpretation of Raman spectra of disordered and amorphous carbon," *Phys. Rev. B* **61**, 14095–14107 (2000).

[45] D. C. Harris, *Symmetry and spectroscopy: an introduction to vibrational and electronic spectroscopy*, 1st ed. (New York: Dover Publications, 1989).

[46] Z. Xu, H. Zhongdu, Y. Song, X. Fu, M. Rommel, X. Luo, A. Hartmaier, J. Zhang, and F. Fang, "Topic Review: Application of Raman Spectroscopy Characterization in Micro/Nano-Machining," *Micromachines* **9**, 361 (2018).

[47] A. Ferrari and D. Basko, "Raman spectroscopy as a versatile tool for studying the properties of graphene," *Nature nanotechnology* **8**, 235–46 (2013).

[48] Z. Ni, Y. Wang, T. Yu, and Z. Shen, "Raman spectroscopy and imaging of graphene," *Nano Research* **1**, 273–291 (2008).

[49] R. Trusovas, G. Račiukaitis, G. Niaura, J. Barkauskas, G. Valušis, and R. Pauliukaite, "Recent Advances in Laser Utilization in the Chemical Modification of Graphene Oxide and Its Applications," *Advanced Optical Materials* **4**, 37–65 (2016).

[50] A. Alyamani and O. Lemine, *FE-SEM Characterization of Some Nanomaterial* 2012), pp. .

[51] S. Khan, *Scanning Electron Microscopy: Principle and Applications in Nanomaterials Characterization* 2018).

[52] T. Kaplas and Y. Svirko, "Direct Deposition of Semitransparent Conducting Pyrolytic Carbon Film," *Journal of Nanophotonics* **6**, 1703– (2012).

[53] Z. Ni, Y. Wang, T. Yu, and Z. Shen, "Raman Spectroscopy and Imaging of Graphene," *Nano Res* **1**, 273–291 (2008).

[54] A. Das, B. Chakraborty, and A. Sood, "Raman spectroscopy of graphene on different substrates and influence of defects," *Bulletin of Materials Science* **31**, 579–584 (2008).

[55] A. Ghalib, PhD thesis 2012).

[56] X. Song, L. Song, X. Chen, and T. Zhang, "The characterization of graphene prepared using a nickel film catalyst pre-deposited to fused silica," *RSC advances* **6**, 22244–22249 (2016).